

Surprisingly High Redundancy in Electronic Structure Data

Sazzad Hossain ¹, Ponkrshnan Thiagarajan ², Shashank Pathrudkar ¹, Stephanie Taylor ³, Abhijeet Sadashiv Gangan ³, Amartya S. Banerjee ^{3,*} and Susanta Ghosh ^{1,4,†}

¹*Department of Mechanical and Aerospace Engineering, Michigan Technological University*

²*Hopkins Extreme Materials Institute, Johns Hopkins University*

³*Department of Materials Science and Engineering, University of California, Los Angeles*

⁴*Faculty member of the Center for Artificial Intelligence, Michigan Technological University*

(Dated: July 15, 2025)

Machine Learning (ML) models for electronic structure rely on large datasets generated through expensive Kohn-Sham Density Functional Theory simulations. This study reveals a surprisingly high level of redundancy in such datasets across various material systems, including molecules, simple metals, and complex alloys. Our findings challenge the prevailing assumption that large, exhaustive datasets are necessary for accurate ML predictions of electronic structure. We demonstrate that even random pruning can substantially reduce dataset size with minimal loss in predictive accuracy, while a state-of-the-art coverage-based pruning strategy retains chemical accuracy and model generalizability using up to 100-fold less data and reducing training time by threefold or more. By contrast, widely used importance-based pruning methods, which eliminate seemingly redundant data, can catastrophically fail at higher pruning factors, possibly due to the significant reduction in data coverage. This heretofore unexplored high degree of redundancy in electronic structure data holds the potential to identify a minimal, essential dataset representative of each material class.

I. INTRODUCTION

The calculation and analysis of the electronic structure of materials underpins much of modern computational materials science. From predicting thermodynamic stability and charge transport to modeling chemical reactivity, the electronic structure serves as a fundamental description of how interacting atoms and electrons give rise to observable properties. Consequently, electronic structure calculations often serve as an important building block of multiscale materials modeling [1] with a significant share of contemporary high performance computing resources being devoted to such simulations [2–4].

Kohn-Sham Density Functional Theory (KS-DFT) serves as the primary workhorse of modern electronic structure calculations [5–7]. Although formulated in terms of the so-called Kohn-Sham orbitals, the fundamental unknown in KS-DFT is the *electron density*. Indeed, many ground state material properties, e.g. structural parameters and elastic constants, may be computed from the electron density field, and it also serves as the starting point for *ab initio* descriptions of excited state phenomena. However, practical calculations using KS-DFT, especially for complex systems such as disordered alloys or materials with extended defects, can be limited by the cubic scaling computational cost of the method with respect to system size. As such, a considerable share of research has been devoted to the development of specialized solution techniques and high performance computing algorithms to overcome this bottleneck [8–16].

In recent years, Machine Learning (ML) has enabled the development of powerful surrogate models that can

enable the prediction of the ground state electron density and related properties at a fraction of the computational cost of conventional first principles simulations [17–28]. These ML models are typically trained on KS-DFT data and use descriptors of the atomic environment to produce the electron density as the output. Recent studies have demonstrated the success of such ML models in predicting electron densities across a wide range of systems, including pure metals, alloys, insulators, organic molecules and nanostructures [19, 20, 26–29]. Moreover, these models show promising extrapolation capabilities, accurately predicting electron densities for unseen compositions in complex alloys, atomic configurations with defects and dislocations, and for chemical species beyond training [27–29]. The ML models have also been continuously improved to address several challenges, including the enforcement of physical symmetries, incorporation of uncertainty quantification capabilities, and improvements in training and prediction efficiency [18, 27, 30].

The paradigm shift brought on by the development of ML based electronic structure techniques has motivated the creation of extensive datasets [31–34] — sometimes comprising millions of structures — under the implicit assumption that large, exhaustive sampling is essential to achieve high predictive accuracy and generalizability [35–37]. While this assumption has driven progress in materials informatics [38–40], it also raises questions about the efficiency and necessity of such data collection efforts, particularly given the computational cost and environmental footprint associated with high-throughput quantum mechanical calculations.

In this work, we examine a fundamental but largely overlooked question: How much of this electronic structure data is genuinely essential? To answer this, we systematically probe the redundancy in electron density data spanning molecular systems, elemental metals, and

* asbanerjee@ucla.edu

† susantag@mtu.edu

complex alloys, and show that a surprisingly small subset is often sufficient to train ML models to within chemical accuracy. Our findings challenge the prevailing view that predictive fidelity and generalizability requires vast amounts of data and suggest that it is possible to identify minimal datasets that dramatically reduce computational cost without sacrificing accuracy. Thus our exploration of the redundancy of electronic structure data can potentially lead to a small foundational dataset for each material class, which in turn can be used for benchmarking and training foundation models.

The exploration of redundancy in chemical datasets has received prior attention in the literature [41–43]. For instance Li et. al. [41] have demonstrated a high degree of redundancy in datasets of scalar material properties such as the formation energy and band gaps, and have proposed an iterative strategy to reduce the size of training data. However, there has not been a systematic exploration of redundancies in the electronic structure itself, particularly in the context of ML models. Notable prior efforts include the observation that electronic structure data for various simple systems often lie on low-dimensional manifolds, enabling reconstruction via low-rank tensors [44, 45] or a small number of principal component modes [26, 30]. Somewhat relatedly, recent contributions have also exploited redundancies in the electron density to develop strategic sampling schemes for grid-based representations [46, 47], although the effectiveness of such approaches may depend sensitively on the manner in which core states are modeled. Thus, although previous studies have addressed redundancy in various contexts, statistically grounded one-shot pruning methods — free from ad hoc heuristics — have yet to be explored for electronic structure data. Accordingly, determining a statistically justifiable level of data redundancy remains an open problem, which we address. Thus, the techniques explored here are applicable to any class of material without the need for domain knowledge and possibly even to fields beyond the electron density.

The observation of redundancy in electronic structure data is closely connected to Kohn’s nearsightedness principle [48, 49]. Indeed, this result has been used to deduce that the single particle density matrix that appears in electronic structure calculations can be very sparse [50, 51], and has led to a large number of electronic structure codes that exploit it [8, 9, 52–59]. In the realm of ML-based electronic structure predictions, similar considerations can be used to motivate the prunability of electronic structure data: since local environments largely determine the electronic structure, many configurations differing only in distant parts of the system are expected to have nearly identical electronic descriptors. This implies substantial redundancy in datasets that exhaustively enumerate configurations, especially in large and complex systems. However, there has not been a systematic exploration of this aspect, particularly in the context of state-of-the-art neural network based ML models of electronic structure.

Neural network performance generally improves with data and model size, often following a power law scaling [60, 61]. However, beyond a certain level, marginal accuracy gains require significantly more data [62, 63]. Thus, power law scaling suggests that much of the training data is redundant and can be pruned without notable performance loss [62]. Commonly used approaches for selecting a smaller, representative subset of a large dataset that preserves ML model performance are referred to as *data pruning* techniques or *coreset selection* methods. These techniques are often broadly categorized into the following three major approaches [64], *importance score* based methods [64–67], *coverage* driven methods [68–70] and *optimization*-based methods [71–75].

Most existing pruning methods have been evaluated primarily on classification problems, whereas electronic structure prediction is a regression task. Therefore, identifying the degree of prunability of electronic structure data, as well as the most suitable pruning technique remain unexplored. In the present work, two state-of-the-art methods: GraNd [65] and Coverage-Centric Coreset Selection (CCS) [68] are adopted. Optimization-based methods are not considered in this work because, despite their strong theoretical foundation and impressive performance, they are computationally quite expensive, and can be challenging to implement on large-scale datasets [76]. The GraNd technique is adopted because of its intuitive approach, ease of implementation, and ability to identify important examples early in the training. GraNd, an *importance-score* based method, assigns lower scores to easy-to-learn examples, which are deemed redundant and removed while pruning. This can lead to poor data coverage at high pruning factors, as only difficult-to-learn examples are retained, causing severe performance drop [68, 77]. CCS, a *coverage*-driven method, overcomes this limitation by proposing a probability density-based distribution coverage strategy to improve the coverage of the coreset [68]. CCS is adopted here due to its exceptional performance at high pruning factors and its flexibility in incorporating any importance score.

Through the use of these data-pruning techniques, we explore the degree of redundancy in electronic structure data across a wide variety of material systems — a metal, a chemically complex disordered alloy system, and molecules. We show that high degrees of redundancy appear to be a generic feature of electronic structure data: even random pruning can substantially reduce dataset size with minimal loss in predictive accuracy, while state-of-the-art coverage-based methods unveil even more dramatic levels of redundancy. Thus, a remarkably large fraction of the dataset across all the materials studied can be systematically pruned while preserving prediction accuracy and model generalizability. We have further quantified the quality of predictions via calculations of the ground-state energy from predicted electron densities and have found that chemically accurate predictions (i.e., energy errors less than 1 kcal/mole or 1.6 mHa/atom)

can be made even after pruning 99% of the data. In particular, our results for complex disordered metallic alloys hold across composition space, thus suggesting the potential to identify a minimal, essential dataset representative of each material class. Additionally, we found that for the materials considered here, ML model training time on the pruned datasets can be reduced by a factor of three or more, thus enabling accelerated hyperparameter tuning and foundation model development.

The remainder of this paper is structured as follows: Section II presents our findings, followed by a discussion in Section III, and methodology details in Section IV.

II. RESULTS

In this section, we quantify the redundancy in electronic structure data for three different materials. We present the error in the ML model for various pruning factors to identify the fraction of data that can be pruned without significantly compromising the model’s performance and generalizability, and further quantify this through the accuracy of the energy computed from the ML-predicted electron density.

The dataset consists of snapshots of KS-DFT simulation taken at intermittent time steps, with each snapshot capturing the atomic coordinates, species information and the resulting electron density over the simulation cell. Given a grid point in the simulation domain, the ML model provides a map to the electron density at that point, from the nearby atomic configuration. Details of the KS-DFT simulations and the ML map are provided in Section IV A.

To explore the redundancy, pruning is performed by removing a subset of the grid points of the original dataset. We explore three approaches for data pruning: random

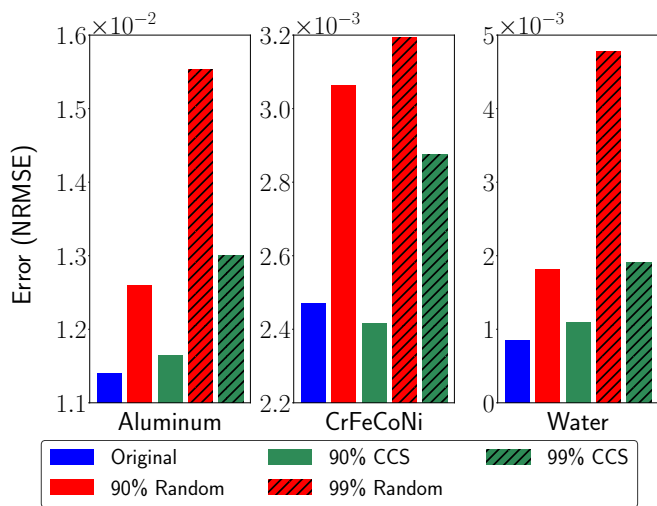


FIG. 1: Error in ML-predicted electron density for the original dataset, randomly pruned dataset, and 90% and 99% CCS-based pruned dataset.

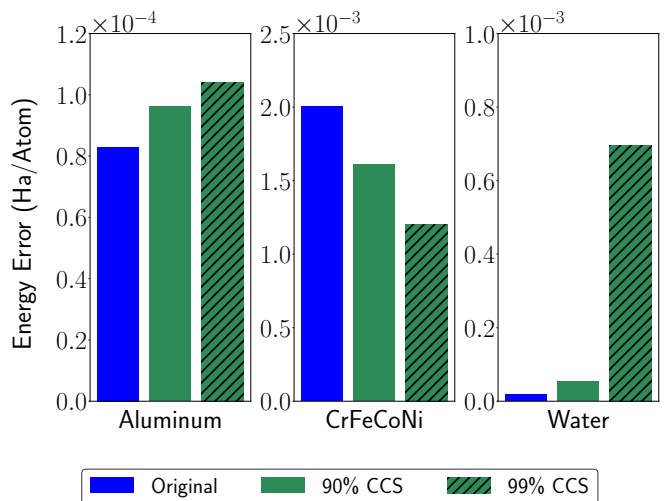


FIG. 2: Error in energy obtained from the ML-predicted electron density for the original dataset, 90% and 99% CCS-based pruned dataset.

grid-point-wise pruning, GraNd score-based pruning, and CCS-based pruning. In random grid-point-wise pruning, grid points from the original dataset are removed randomly. The importance score (i.e. GraNd score) is computed for each datapoint and used for the GraNd and CCS approaches. Upon training ML models on the pruned datasets, the errors in the predicted electron density on a testing dataset are computed. We report the commonly used normalized root mean squared error (NRMSE) [30] as and error metric, defined in the supplemental materials V A.

Figure 1 highlights the redundancy in electronic structure data. For all three systems, 90% of the data can be pruned through the CCS-method, without compromising accuracy in the predicted electron density. Even 99% redundancy can be identified by the CCS method: at such a high pruning factor, the errors increase as expected, but the predicted electron densities still result in chemically accurate energies (i.e., errors less than 1 kcal/mole or 1.6 mHa/atom) across all system, as shown in Figure 2. Notably, while the errors in the electron density and the corresponding energy errors are correlated, the one-to-one relationship between them can break down when the density errors and hence the energy errors are themselves low. This situation can arise for low pruning percentages across all models, or for very high pruning percentages, for some models. An additional issue to keep in mind is that in general, the CrFeCoNi alloy system is more difficult to predict accurately through ML models, because of the involvement of harder pseudopotentials and semi-core electrons for transition metals in the KS-DFT calculations, and the large amount of compositional variation [28]. Thus, the overall ML predictions are slightly less accurate for this system, as opposed to the other systems studied here. However, our key finding, in this regard is that there is still a high degree of redundancy

in the CrFeCoNi electronic structure data, and the elimination of this redundancy does not reduce ML model prediction accuracy further.

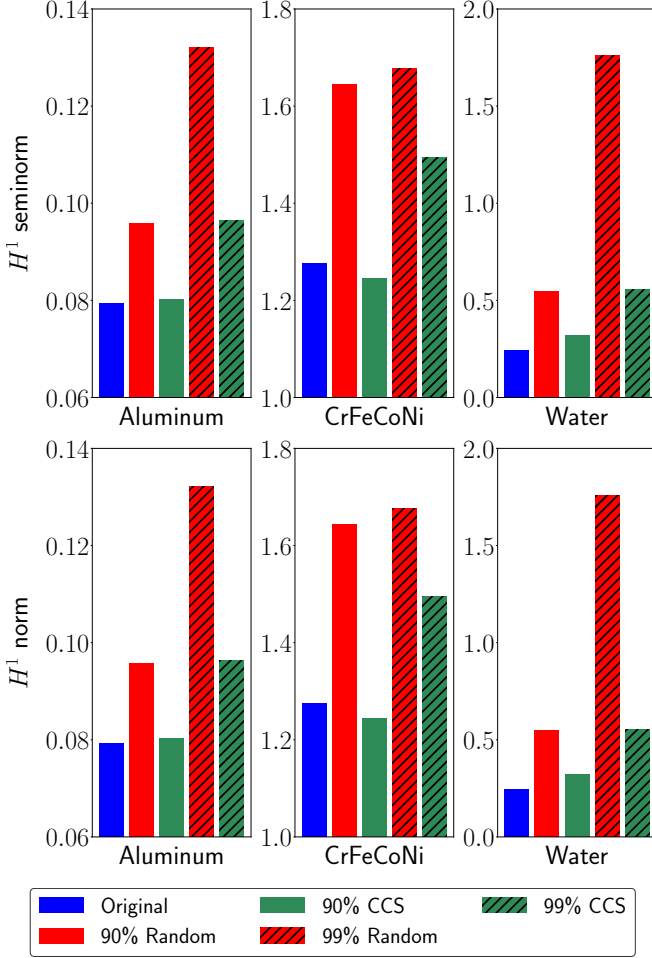


FIG. 3: (a) H^1 seminorm and (b) H^1 norm of the error for the ML-predicted electron density obtained from the original, 90% CCS and 99% CCS based pruned dataset.

To demonstrate that the ML models not only capture the electron density field but also smooth spatial variations in it, we plot the H^1 seminorm and H^1 norm of the error in electron density field in Figure 3 (see the supplemental materials V A for further details). We see a trend very similar to what is seen in Figure 1. For all the three material systems, the 90% CCS dataset achieves H^1 seminorm and H^1 norm values similar to the original dataset, whereas 99% CCS dataset shows a slight increase. The 90% and 99% random pruning dataset has a higher H^1 seminorm and H^1 norm than CCS based pruning for all three systems.

In the following, we present the detailed performance of the pruning techniques for various pruning factors using aluminum, CrFeCoNi, and water as representative examples of a metal, a complex alloy system, and molecule, respectively.

A. Aluminum

We find that just 10% of the data for Aluminum systems can be selected through the CCS method to match the performance of the original dataset. Moreover, even 1% of the data can be selected to yield a remarkably accurate ML model, that maintains chemical accuracy in the energies.

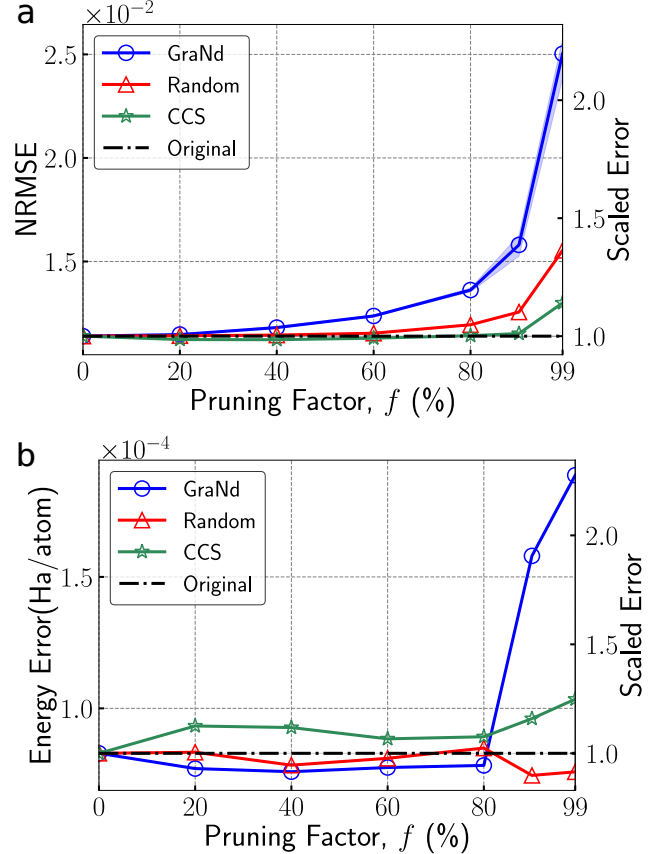


FIG. 4: **Aluminum system:** (a) The error in the electron density prediction for various pruning factors. The shaded region represents the range (maximum to minimum) of three ML models around the mean, shown by a solid line. (b) The error in energy obtained from the predicted electron density for various pruning factors.

The errors (NRMSE) in electron density predictions for the three pruning approaches — random, GraNd, and CCS — are plotted against various pruning factors in Figure 4(a). GraNd, random, and CCS perform nearly as well as the original dataset up to 40%, 80%, and 90% pruning, respectively. The performance of the GraNd technique deteriorates more rapidly than random and CCS techniques. The exceptional performance of CCS at higher pruning rates, such as 80% and 90%, is evident, with the increase in NRMSE compared to the original dataset being only 0.7% and 2.1%, respectively. CCS also performs surprisingly well at 99% pruning (i.e. two

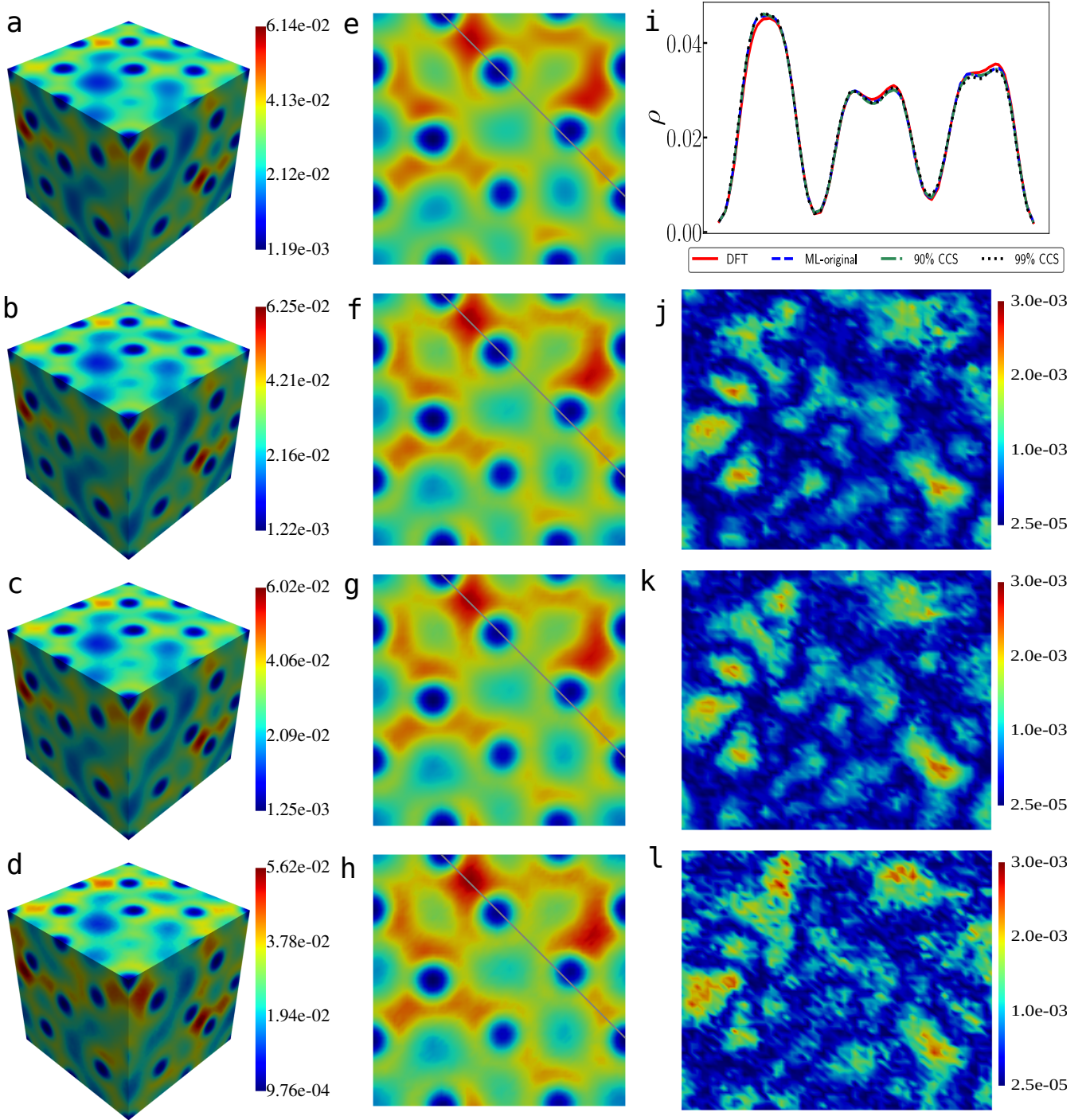


FIG. 5: **Aluminum system at 1500K.** Electron density obtained by: (a) DFT and (b-d) ML model for original, 90% CCS and 99% CCS. (e-h) A two-dimensional (2D) slices of the simulation cell corresponding to Figures (a-d) showing electron density. (i) Electron density along the solid line, shown in Figures (e-h). (j-l) Absolute error in ML-predicted electron density for original, 90% CCS, and 99% CCS corresponding to Figures (f-h). The unit of electron density is $e \cdot \text{Bohr}^{-3}$, where e denotes the electronic charge.

orders of magnitude less data), showing only a nominal increase in NMRSE.

To assess the quality of the prediction further, the total energy of the system is calculated from the ML-predicted electron density, via postprocessing. The total energy error (Hartree/atom) relative to the KS-DFT calculations, are shown in Figure 4(b). This is essential in understanding if it is possible to maintain chemical accuracy in the energies computed from the electron density predictions of ML models trained on pruned data. All three methods maintain near-original accuracy in the energy up to 80% pruning. In particular, all three techniques maintain chemical accuracy even at 99% pruning, with the CCS and random pruning techniques surpassing the accuracy of the GraNd technique at such high pruning fractions.

To compare the accuracy of the ML models against KS-DFT over the entire spatial domain, we plot the ML predicted electron density fields as obtained using original dataset, the 90% CCS dataset, and the 99% CCS dataset, in Figure 5(a-h). All three ML models show excellent agreement with the DFT calculations. The error fields of the ML model predictions with respect to the KS-DFT simulations are shown in Figure 5(j-l), which confirms that the error for 90% or 99% CCS does not show significant increase compared to the original ML model. The electron density along the solid line shown in figures (e-h) is plotted in Figure 5(i). The details of the 3D error fields is also shown via iso-surfaces in the supplemental materials V H, Figure 21, which shows negligible increase in error for 90% and 99% pruned data.

B. CrFeCoNi Alloy

We find that just 10% of the data, selected through the CCS method, can match the performance of the original dataset while 1% of the data can be selected to yield a exceptionally accurate ML model, that maintains chemical accuracy in the energies.

The errors (NRMSE) in electron density predictions for three pruning approaches — random, GraNd and CCS — are plotted against various pruning factors in Figure 6(a). Random, GraNd, and CCS methods perform nearly as accurately as the original dataset up to 40%, 60% and 90% pruning, respectively. The performance of GraNd-based pruning drops catastrophically at higher pruning rates, far more rapidly than random pruning or CCS. Indeed, the exceptional performance of the CCS method is evident even at higher pruning rates, such as 80% and 90%, with the variations in errors being less than 1% as compared to the original dataset. CCS also performs very well at 99% pruning (i.e. two orders of magnitude less data), showing a slight increase in the error (NRMSE).

The quality of ML-predicted electron densities are further assessed through post-processing calculations to obtain the total energy of the system. The total energy error (Hartree/atom) relative to KS-DFT calculations are

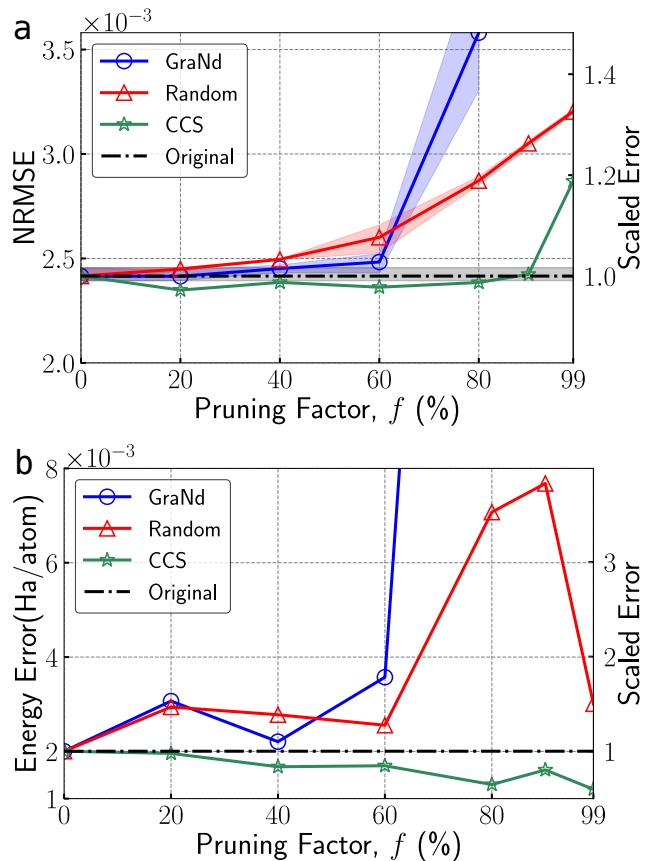


FIG. 6: **CrFeCoNi system:** (a) Error in the electron density prediction for various pruning factors. (b) Error in energy obtained from the predicted electron density for various pruning factors.

shown in Figure 6(b). This is essential in understanding if it is possible to maintain chemical accuracy in energies from the electron density predictions based on the pruned datasets. All methods maintain near-original accuracy in the energy up to 60% pruning. In particular, the CCS approach provides near original accuracy up to 99% while maintaining chemical accuracy in the energies, and surpassing both random pruning and GraNd, even at such a high pruning rate. Notably, the fluctuations in the energy errors of the original, 90% and 99% pruned datasets are consistent with observations made in ML predictions of the electronic structure of quaternary systems in our recent work [28].

An unscaled version of Figure 6 can be found in the supplemental materials V C, Figure 14. To compare the accuracy of the ML models against the KS-DFT over the spatial domain, we plot the ML-predicted electron density fields obtained using the original dataset, 90% CCS dataset and 99% CCS dataset, in Figure 7. All three models show remarkable agreement with the DFT calculations. The absolute error in the fields of ML predictions with respect to the KS-DFT calculations are plotted in Figure 7(j-l). The errors in 90% CCS pruned dataset

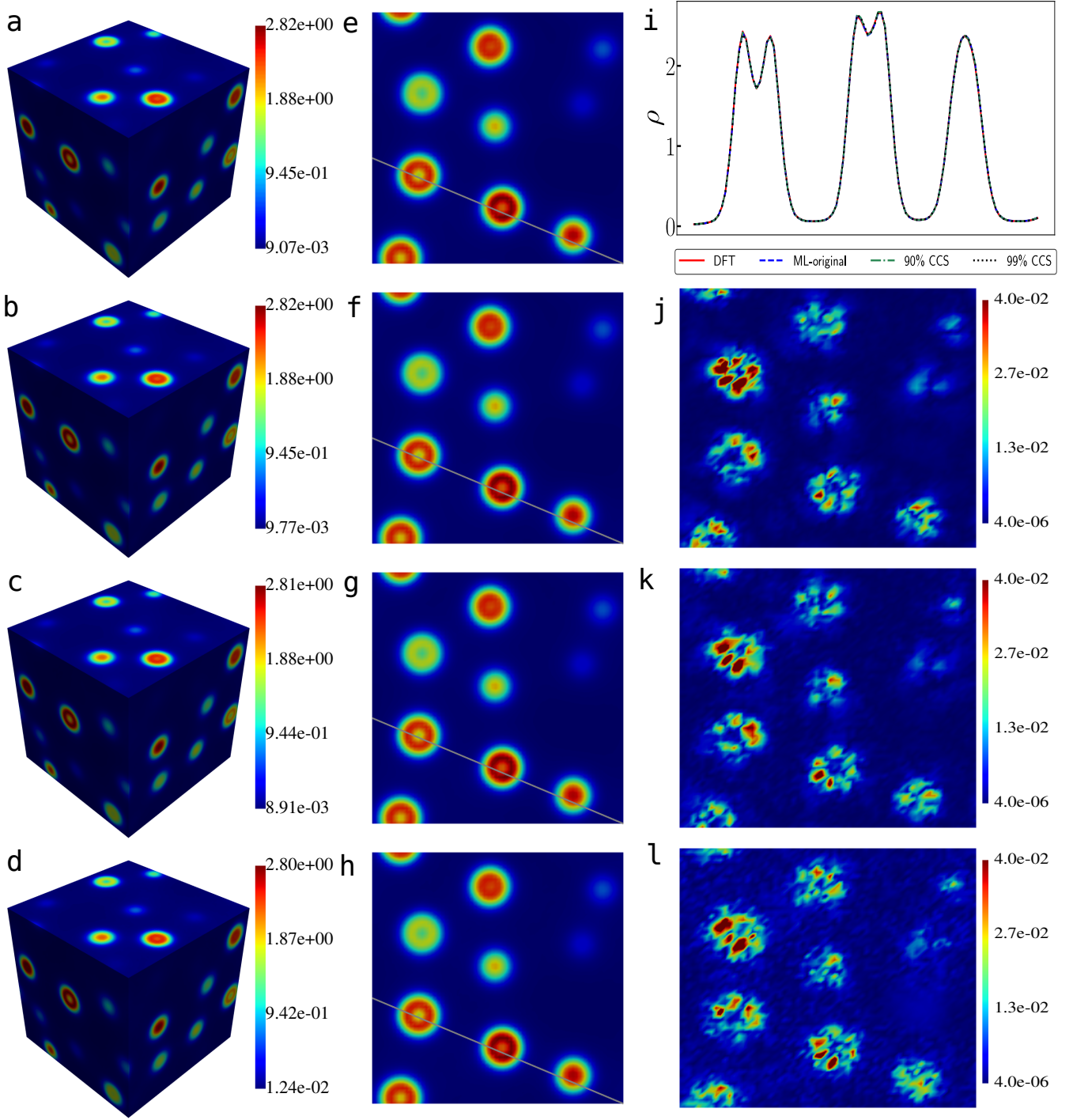


FIG. 7: $\text{Cr}_{25}\text{Fe}_{25}\text{Co}_{25}\text{Ni}_{25}$ alloy system at 5000 K: Electron density obtained by: (a) DFT and (b-d) ML model trained on the original dataset, 90% CCS and 99% CCS based pruned dataset. (e-h) Two-dimensional (2D) slices of the simulation cell corresponding to Figures (a-d). (i) Electron density along the solid line, shown in Figures (e-h). (j-l) Absolute error in ML-predicted electron density for original dataset, 90% CCS-based pruned dataset, and 99% CCS-based pruned dataset. The unit of electron density is $e \cdot \text{Bohr}^{-3}$, where e denotes the electronic charge.

(see Figure 7(k)) are very much similar to the errors in the original dataset (see 7(j)). With 99% pruning, (see Figure 7(l)), the error intensifies slightly throughout the slice. The electron density along the solid line shown in Figure 7(e-h) is plotted in the Figure 7(i). The details of the 3D error fields is also shown via iso-surfaces in the supplemental materials V H, Figure 23, which shows negligible increase in error for 90% and slight increase for 99% pruned data.

C. Water

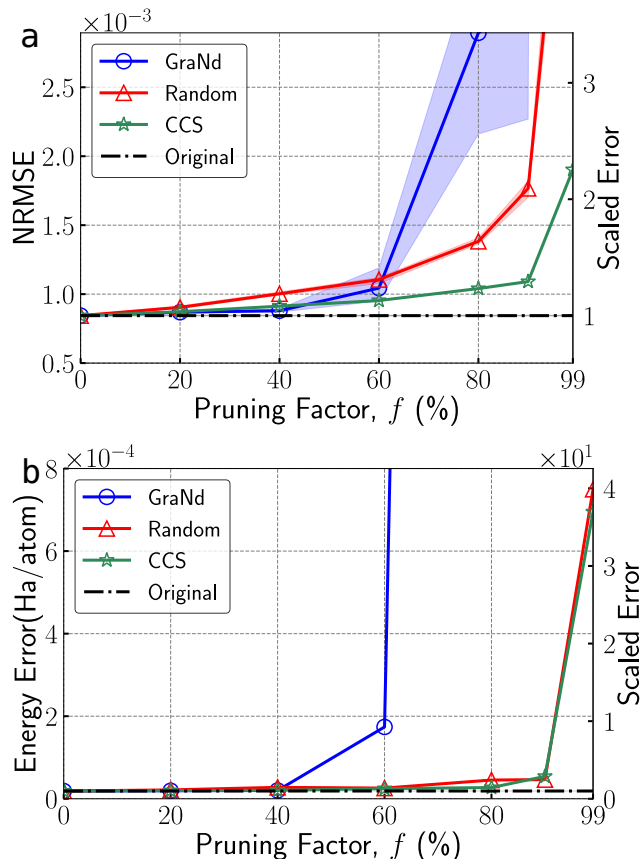


FIG. 8: **Water system:** (a) Error in the predicted electron density for various pruning factors. (b) Error in energy obtained from the predicted electron density for various pruning factors.

We find that just 10% of the data for the water systems, selected through CCS, can match the performance of the original dataset while 1% of the data can be selected using CCS approach to obtain a very accurate ML model, that maintains chemical accuracy.

The errors (NRMSE) in the three pruning approaches—random, GraNd and CCS are plotted in the Figure 8(a). GraNd, random and CCS performs nearly as accurate as the original dataset up to 60%, 60% and 90% pruning. The performance of the GraNd pruning drops rapidly

as compared to the random and CCS methods, which is consistent with the other systems studied here. The exceptional performance of CCS at higher pruning rates, such as 80% and 90% is evident with the increase in error compared to the original dataset being only 23% and 30% respectively. CCS also performs surprisingly well for 99% pruning, but showing a modest increase in error.

The quality of the predictions are further assessed through the post-processing calculations of the energy of the system, obtained from the ML-predicted electron density. The total energy error (Ha/atom) relative to KS-DFT calculations is shown in Figure 8(b). This allows us to quantify the quality of the ML-predicted electron density for all the pruning factors and is essential for understanding if it is possible to maintain chemical accuracy in energies from ML-predicted electron densities that were trained on pruned datasets. All methods maintain near-original accuracy in the energy up to 40% pruning maintaining chemical accuracy levels. In particular, the random pruning and CCS approach provide near original accuracy up to 90% while maintaining chemical accuracy level in the energies surpassing GraNd at such high pruning rate. An unscaled version of Figure 8 is provided in the Supplemental Materials V C, Figure 15.

To compare the accuracy of the ML models against the KS-DFT over the spatial domain, we plot the ML-predicted electron density fields obtained using the original dataset, 90% CCS dataset, and 99% CCS dataset in Figure 9. All three models show remarkable agreement with the DFT calculations. The absolute error in the fields of ML predictions with respect to the KS-DFT calculations are plotted in Figure 9(j-l). The errors in the 90% CCS pruned dataset (see Figure 9(k)) are very similar to the errors in the original dataset (see Figure 9(j)). With 99% pruning (see Figure 9(l)), the error intensifies slightly throughout the slice. The electron density along the solid line shown in Figure 9(e-h) is plotted in Figure 9(i). The details of the 3D error fields are also shown via iso-surfaces in supplemental materials V H, Figure 25, which shows a negligible increase in error for 90% pruning and a slight increase for 99% pruned data.

D. Generalizability of the ML models

The limited generalization capability of ML models beyond their training data remains a fundamental issue of the field. In particular, the generalization capability of ML models developed using pruned data is yet unexplored. To address this issue, we evaluate the generalization capabilities of the ML models developed here, by assessing their performance on a diverse set of systems that differ significantly from, and were not included in, the training data. These test cases include systems with structural defects such as mono- and di-vacancies, even though the models were trained exclusively on defect-free systems.

The ML-predicted densities via CCS (90% and 99%

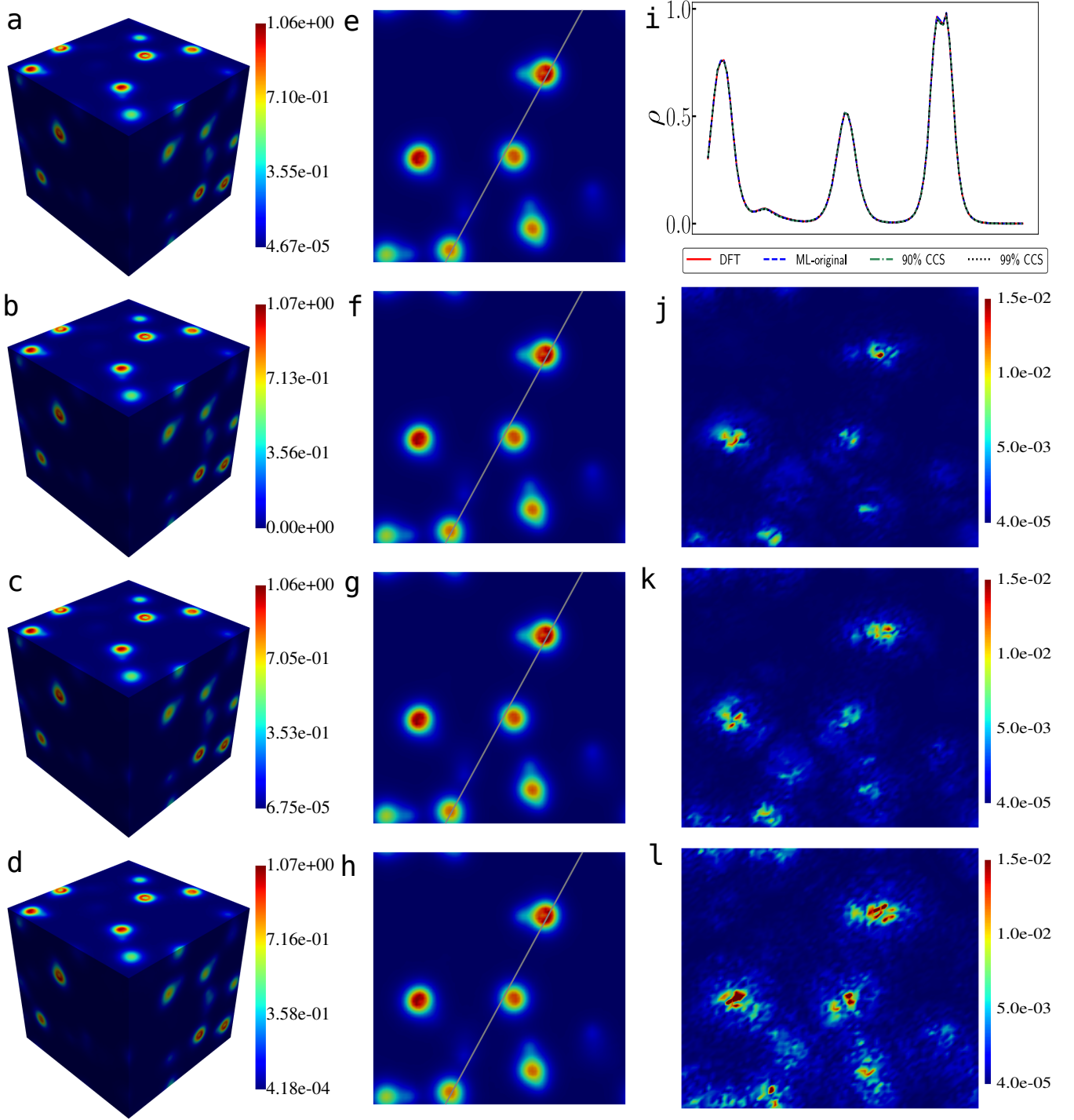


FIG. 9: **Water system at 600K:** Electron density obtained by: (a) DFT and (b-d) ML model trained on the original dataset, 90% CCS and 99% CCS based pruned dataset. (e-h) Two-dimensional(2D) slices of the simulation cell corresponding to figures (a-d). (i) Electron density along the solid line, shown in Figures (e-h). (j-l) Absolute error in ML-predicted electron density for the original dataset, 90% CCS-based pruned dataset, and 99% CCS-based pruned dataset. The unit of electron density is $e \cdot \text{Bohr}^{-3}$, where e denotes the electronic charge.

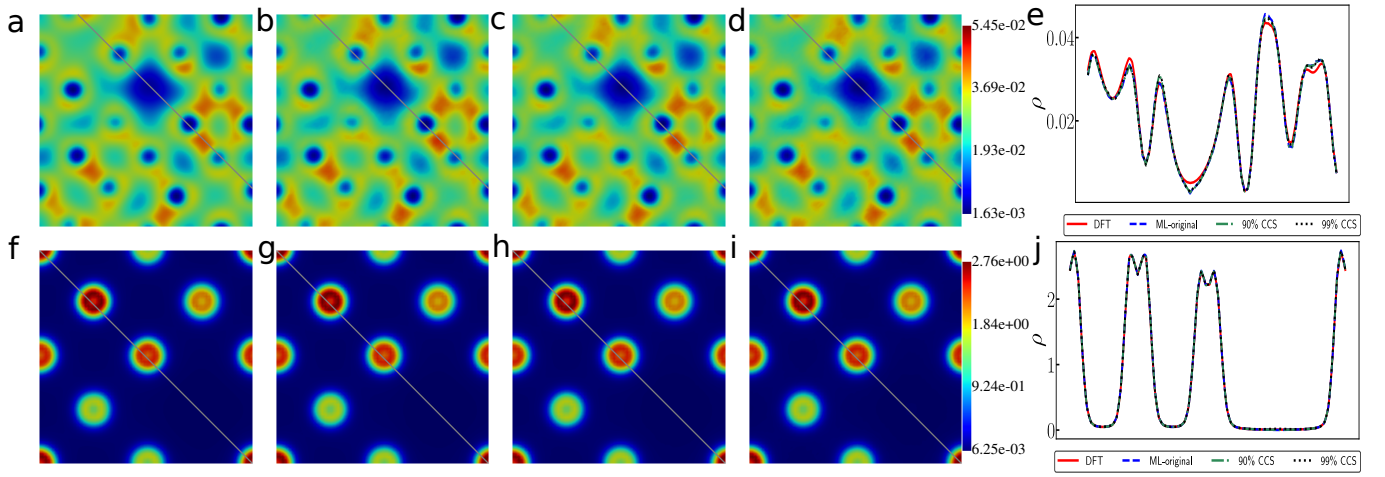


FIG. 10: **Model generalizability to unseen defect configurations:** (*Top*) Mono-vacancy defect for Aluminum 108 atoms systems. Two-dimensional(2D) slices of electron density obtained by: (a) DFT and (b-d) ML model trained on the original dataset, 90% CCS and 99% CCS based pruned dataset. (e) Electron density along the solid line, shown in Figures (a-d). (*Bottom*) Mono-vacancy defect for CrFeCoNi 32 atoms systems. 2D slices of electron density obtained by: (f) DFT and (g-i) ML model trained on the original dataset, 90% CCS and 99% CCS based pruned datasets. (j) Electron density along the solid line, shown in Figures (f-i). The unit of electron density is $e \cdot \text{Bohr}^{-3}$, where e denotes the electronic charge.

pruning) exhibit remarkable agreement with KS-DFT across all test systems, including both aluminum and CrFeCoNi alloys. Moreover, the prediction errors for defective systems, e.g. mono-vacancy, are comparable in magnitude to those observed for pristine systems, as illustrated in Figure 10. Importantly, the generalization capability of the ML models remains unaffected by upto two orders of magnitude CCS-based pruning. Additional comparisons between ML-predicted and KS-DFT-computed electron density fields for various pruning factors, including the di-vacancy defect for the aluminum system and the CrFeCoNi system, are presented in the Supplemental Material V E.

III. DISCUSSION

We have explored the hidden redundancy in electronic structure datasets for diverse material systems. To the best of our knowledge, this marks the first exploration of redundancy in electronic structure datasets through systematic pruning approaches. In addition to random pruning, we have employed two ML-based pruning techniques, namely GraNd [65] and CCS [68]. GraNd based pruning selects a subset of data having the highest importance scores. The CCS approach selects a subset that ensures comprehensive coverage of the dataset based on a probability density based data distribution coverage. These two ML based pruning methods are compared against random grid-point wise pruning — with the goal of revealing the aforementioned redundancy, and helping select the minimal essential dataset without compromising accuracy. Overall, we are able to identify a large fraction of the electronic structure data that is redundant and which can be eliminated from ML training, without compromising the accuracy or the smoothness of the ML predicted fields.

Random grid-point-wise pruning turns out to be an effective strategy, aligning with findings in the computer vision literature. Although its error rate increases at higher pruning levels, it can outperform several ML-based pruning methods [68, 77].

For all three material systems, at lower pruning rates, GraNd captures the redundancy of the dataset effectively, closely matching or outperforming the original dataset. However, at higher pruning rates, GraNd’s performance drops catastrophically. This occurs because, at large pruning factors, most of the easy-to-learn data points are removed, significantly altering the data distribution and leading to poor data coverage.

We found that pruning via CCS consistently outperforms the other two methods, particularly at higher pruning factors. It can systematically identify an order of magnitude smaller subset of the dataset that maintains the performance of the original dataset (i.e., it is practically *lossless*) for all materials studied here. We have also verified this trend via computing the system’s energy from the ML-predicted electron densities. Further-

more, pruned data sets which are two orders of magnitude smaller than the original (i.e., 99% pruning fraction) also demonstrate surprisingly high accuracy, and result in chemically accurate energy predictions.

We also demonstrate that 90% and 99% CCS based pruned datasets retain significant generalization capability of the model, through tests on mono- and divacancies.

In addition to identifying the essential subset of the data, pruning can also accelerate ML model training due to the reduced size of the subset. We found that for the materials considered here, ML model training time on the pruned datasets can be lower by 50% – 80%, as compared to the training time on unpruned data (See Section V G of the supplemental material). Thus, such pruned datasets can be used to accelerate hyperparameter tuning. In turn, these advancements can be critical in developing ML models that work across chemical space.

IV. METHODS

The electron density data needed for training, validation, and testing of the ML models was produced via Kohn-Sham Density Functional Theory (KS-DFT) calculations [5, 78] as implemented in the finite-difference based SPARC code [79–81]. Norm conserving (ONCV) pseudopotentials [82–84] and GGA PBE exchange-correlation [85] were employed. Prior to using the pseudopotentials for electronic structure data generation, tests were performed to verify that lattice parameters and other physical quantities predicted were consistent with the literature and that the energies and forces were sufficiently converged with respect to the mesh fineness. The mesh spacing chosen for the aluminum, CrFeCoNi, and water systems were 0.25, 0.20, and 0.25 Bohr respectively. A tolerance of 10^{-6} was chosen for the self-consistent field (SCF) iteration convergence, and the Periodic-Pulay scheme [86] was employed for convergence acceleration. The KS-DFT calculations for ML data generation only sampled the gamma point in reciprocal space, as is common in the simulation of large condensed matter systems.

While the aforementioned calculations provided the electron densities for a given atomic configuration, additional techniques were employed to efficiently generate a large sample set of atomic configurations. For the aluminum system, *Ab Initio* Molecular Dynamics (AIMD) simulations were employed, and the electron density data needed for the ML models was extracted from AIMD “snapshots” at regular simulation intervals [19, 27]. A standard Nosé Hoover thermostat [87] with temperatures between 298 K and 2100 K was employed, and with Fermi-Dirac smearing at a fixed electronic temperature of 631.554 K was used. As pointed out in our recent contributions, use of thermalized systems to sample the configuration space leads to more generalizable ML models of the electronic structure [27, 28], due to better sampling of the input features space.

While AIMD simulations are convenient for data gen-

eration, they are computationally costly. In order to reduce the data generation expense for the water and CrFeCoNi alloy systems, atomic configurations were generated through classical Molecular Dynamics (MD) simulations employing machine learning based interatomic potentials [28]. No accuracy is sacrificed by this method choice since the electron densities corresponding to each configuration are still produced from high-fidelity KS-DFT calculations. At the same time, by running these classical MD simulations at elevated temperatures and over long times, a wide variety of the atomic configurations can be conveniently generated by sampling the resulting MD trajectories. We employed the Materials Graph Library (MatGL) python package [88, 89], which includes the Materials 3-body Graph Network (M3GNet) — a universal machine-learned interatomic potential — for these purposes. The NVT ensemble with Nosé Hoover thermostat was employed for these MD runs as well. The CrFeCoNi alloy data was collected from high-temperature simulations between 2500 K and 7000 K, while the water data was obtained from simulations with temperatures between 300 K and 600 K.

The timestep for both AIMD and MD simulations was set to 1 femtosecond. After a brief simulation period to allow the system to thermally equilibrate, atomic configurations (and also the corresponding electron densities, in case of AIMD) were sampled from the simulation trajectories. Additionally, a number of different initial configurations were used to seed these simulations, in order to allow a larger variety in atomic configurations to be sampled.

A. Machine learning map for electron density prediction

ML approaches for predicting electron densities use descriptors that encode the atomic configuration of a local spatial neighborhood as input. Effective descriptors include interatomic distances and angles, as well as the Superposition of Atomic Densities (SAD), both of which have been successful in capturing local atomic environments [20, 27–29]. The output of these ML models, the electron density, is commonly represented in one of two ways: (1) as sums of atom-centered basis functions [90, 91], which offer computational efficiency but may struggle with complex densities, and (2) as grid-based predictions [19, 21], which provide higher accuracy but require significant computational resources due to fine-mesh evaluations.

The present ML model predicts the ground state electron density values at a set of grid points within a computational domain, based on the coordinates and atomic numbers of the atoms. The mapping is computed in two steps: *First*, atomic neighborhood descriptors are derived for each grid point using the atomic coordinates and species information. *Second*, a neural network is employed to map these descriptors into the corresponding

electron density at each grid point.

As proposed in our recent contribution [28], we adopt the position vectors of atoms in body-attached local frames and the atomic species as the descriptors. This formulation ensures that the descriptors are invariant with respect to rotations, translations and species permutations of the system. Moreover, as shown in [28] the descriptors maintain approximately the same descriptor-vector size even if the number of species in the system increases, thus ensuring efficient representation of atomic neighborhoods across chemical space. The local frame of reference for calculating the descriptors is obtained using Principal Component Analysis (PCA) of an atomic neighborhood consisting of M atoms. The components of the position vector (\mathbf{r}_j) of the j -th atom in the local reference frame are denoted by (x, y, z) . The species information is encoded by using the atomic number of the species. The atomic number of the j -th atom is denoted as Z_j . Thus the descriptors for i -th grid point ($\mathcal{D}_i \in \mathbb{R}^{5M}$) are given as,

$$(\mathcal{D}_i)^j = \left\{ Z_j, \|\mathbf{r}_j\|, \frac{x}{\|\mathbf{r}_j\|}, \frac{y}{\|\mathbf{r}_j\|}, \frac{z}{\|\mathbf{r}_j\|} \right\}; j = 1, \dots, M \quad (1)$$

B. Pruning strategies

We briefly recapitulate the pruning strategies used in this work in addition to the random pruning: first, the GraNd score-based pruning [62, 65], followed by a Coverage-centric Coreset Selection (CCS) method [68] applied to the GraNd scores.

1. Random pruning:

In the present work, a group of grid points from all KS-DFT snap-shots are randomly selected and pruned away. Note that grid points are randomly pruned instead of individual snap-shots.

2. GraNd score based pruning:

We consider a supervised regression setting, where the training set is $S = (x_i, y_i)_{i=1}^N$, drawn i.i.d. from an underlying distribution P . Here, $x_i \in \mathbb{R}^d$ and $y_i \in \mathbb{R}^+$ denote the descriptors at i -th grid point and the electronic charge density at that grid point, respectively. Furthermore, d is the dimension of the atomic-neighborhood descriptors. For a fixed neural network, let the \mathbf{w} be the weights and l be the loss of the neural network at a given step. Let $\mathbf{w}_0, \mathbf{w}_1, \dots, \mathbf{w}_T$ be iteratively updated weights of the neural network, where, for some sequence of minibatches $S_0, S_1, \dots, S_{T-1} \subseteq S$ of size M , we have $\mathbf{w}_t = \mathbf{w}_{t-1} - \eta \sum_{(x,y) \in S_{t-1}} g_{t-1}(x, y)$. Here

$g_t(x, y) = \nabla_{\mathbf{w}_t} l(x, y)$, $t = 1, \dots, T$, and η is the learning rate. The iterations can be perceived as time evolution, with the time derivative of the loss denoted by, $\Delta_t((x, y), S_t) = -\frac{dl}{dt}$. Due to the random initialization of the neural network, the weight vector at time $t > 0$, \mathbf{w}_t , is considered as a random variable.

GraNd score: The GraNd score of a training example (x, y) is defined at time t as $\chi_t(x, y) = \mathbb{E}_{\mathbf{w}_t} \|g_t(x, y)\|_2$, [65]. It represents the impact of removal of an example (x_j, y_j) from the training set (S) on the change in the loss for other examples. The change in the time derivative of the loss of any example (x^*, y^*) resulting from the removal of a training example (x_j, y_j) from the dataset S is bounded by the *GraNd score* associated with the removed example. Formally, for all (x^*, y^*) , there exists a constant c such that $\|\Delta_t((x^*, y^*); S) - \Delta_t((x^*, y^*); S_{-j})\| \leq c \|g_t(x_j, y_j)\|$. Where $S_{-j} = S \setminus \{(x_j, y_j)\}$ and $\Delta_t((x^*, y^*); S) = -\frac{dl}{dt}$. The constant c does not depend on the training examples, (x, y) s. Therefore, the contribution of an example (x, y) to change in the loss of any other example (x^*, y^*) is bounded by the gradient norm, $\|g_t(x_j, y_j)\|$, at any time t , given the weights \mathbf{w}_t . In practice, the gradient of the loss, l , is computed with respect to the model's weights \mathbf{w}_t at epoch t for each training example. The GraNd score is obtained by computing the expectation over several training runs of L_2 norm of the gradient. The examples are ranked based on their GraNd scores, with higher scores indicating greater difficulty in learning.

3. Coverage-centric Coreset Selection

The purpose of coreset selection is to choose a subset (S') of the data (S) that minimizes the loss on the test set [68]. This selection process can be represented through the following optimization problem [69]:

$$\min_{S' \subseteq S: \frac{|S'|}{|S|} \leq 1-f} \mathbb{E}_{x, y \sim P} [l(x, y; h_{S'})], \quad (2)$$

where l is the loss function, $h_{S'}$ is the model trained with the coreset S' , and f is the pruning factor. In other words, S' is a subset of S which has a size at most $(1-f)$ of S , and which minimizes the expected test loss over the distribution P .

In a classical coverage setting, a set S' is called an r -cover set of S if a ball of radius r centered at each data point of S' covers the entire S . Zheng et al. [68] extended the classical geometric set cover to cover a probability distribution—referred to as the *density-based distribution cover*. The associated coreset selection method is called the *Coverage-centric Coreset Selection* (CCS). They also introduced the concept of a partial cover percentage p , of the probability distribution P , instead of the full cover.

A subset S of a metric space (X, d) is defined as the p -partial r -cover of a distribution P , on the space X if:

$$\int_X \mathbf{1}_{\cup_{x \in S} B_d(\mathbf{x}, r)}(\mathbf{x}) d\mu(\mathbf{x}) = p$$

Here $B_d(\mathbf{x}, r) = \{\mathbf{x}' \in X : d(\mathbf{x}, \mathbf{x}') \leq r\}$ denotes a r -radius ball centered at \mathbf{x} , p quantifies coverage (in percentage), and μ represents the probability measure associated with the probability distribution P . The probability density information over the input space is reflected in the measure μ . The percentage of coverage p increases with the increasing radius r for a given set S and a distribution P . Given a coverage percentage p and a set S , the minimum covering radius r is the smallest value such that S achieves at least p percentage coverage under distribution P . In practice, the distribution P is unknown and so an approximate estimation of the coverage is required. Thus, the area under the p-r curve (AUC_{pr}), is proposed as a metric to assess the coverage of a coreset [68]. The quantity AUC_{pr} defined as the expectation of the minimum distance between the examples that follows the distribution P and the data in S : $\text{AUC}_{pr}(S) = \mathbb{E}_{x \sim P} [\min_{x' \in S} d(\mathbf{x}', \mathbf{x})]$. The lower the value of the AUC_{pr} , the better the coverage by the coreset.

State-of-the-art methods often tend to eliminate low-importance data points from high-probability density regions, which decreases coverage (increases the AUC_{pr}), and in turn, this can degrade model performance under high pruning rates. In our implementation of CCS, we used the GraNd score as the importance score. However, the coverage obtained by CCS is distinct from that obtained by GraNd based pruning alone. Traditional GraNd removes only low-scoring examples, leading to poor coverage. In contrast, CCS maintains better data coverage in high-probability density regions, reducing AUC_{pr} and improving performance, even under significant pruning. CCS allocates more sampling budget to high-probability density areas with easy examples, improving coverage of the data distribution. Compared to random sampling, CCS allocates more resources to low-probability density regions, focusing on challenging examples that are critical for training.

CCS steps: Consider a dataset $S = \{(x_i, y_i, s_i)\}_{i=1}^n$ where s_i is the importance score for i -th example (x_i, y_i) . First, CCS selects a pruning rate β , a tunable hyperparameter representing the percentage of hard examples to remove. Pruning $\beta\%$ of hard examples from S yields S_o . Second, CCS partitions S_o into k strata based on importance (GraNd) scores, using fixed-width score intervals. While each stratum has the same score range, the number of examples per stratum may vary. Third, given the pruning factor f , the desired coreset size is determined as $m = (1-f)n$. This total budget m is distributed evenly across the k strata (another hyperparameter), allocating m/k samples per stratum. If a stratum has fewer examples than its budget, all its examples are included. The final coreset (S') is formed by combining the sampled examples from all strata.

Author contributions

SH, PT and SP worked on developing the framework for pruning and other machine learning aspects. ST and AG worked on the DFT data generation and post-processing calculations. ASB and SG were involved in conceptualization, methodological design, supervision, and securing funding/resources. All authors contributed to writing the manuscript.

Competing Interests

The authors declare no competing interests.

Data Availability

Raw data were generated at Hoffman2 High-Performance Compute Cluster at UCLA's Institute for Digital Research and Education (IDRE) and National Energy Research Scientific Computing Center (NERSC). Derived data supporting the findings of this study are available from the corresponding author upon request.

Code Availability

Codes supporting the findings of this study are available from the corresponding author upon reasonable request.

ACKNOWLEDGMENTS

This work was primarily supported by grant DE-SC0023432 funded by the U.S. Department of Energy, Office of Science. This research used resources of the National Energy Research Scientific Computing Center, a DOE Office of Science User Facility supported by the Office of Science of the U.S. Department of Energy under Contract No. DE-AC02-05CH11231, using NERSC awards BES-ERCAP0033206, BES-ERCAP0025205, BES-ERCAP0025168, and BES-ERCAP0028072. SG acknowledges the grant 2442313 funded by the U.S. National Science Foundation. The authors would like to thank UCLA's Institute for Digital Research and Education (IDRE), the MRI GPU cluster at MTU for making available some of the computing resources used in this work. The authors acknowledge the use of the GPT-4o (OpenAI) model to polish the language and edit grammatical errors in some sections of this manuscript. The authors subsequently inspected, validated and edited the text generated by the AI model, before incorporation.

-
- [1] E. B. Tadmor and R. E. Miller, *Modeling materials: continuum, atomistic and multiscale techniques* (Cambridge university press, 2011).
 - [2] J. Hafner, *Journal of computational chemistry* **29**, 2044 (2008).
 - [3] S. Curtarolo, G. L. Hart, M. B. Nardelli, N. Mingo, S. Sanvito, and O. Levy, *Nature materials* **12**, 191 (2013).
 - [4] K. Lejaeghere, G. Bihlmayer, T. Björkman, P. Blaha, S. Blügel, V. Blum, D. Caliste, I. E. Castelli, S. J. Clark, A. Dal Corso, *et al.*, *Science* **351**, aad3000 (2016).
 - [5] W. Kohn and L. J. Sham, *Physical review* **140**, A1133 (1965).
 - [6] P. Hohenberg and W. Kohn, *Physical review* **136**, B864 (1964).
 - [7] J. Hafner, C. Wolverton, and G. Ceder, *MRS bulletin* **31**, 659 (2006).
 - [8] V. Gavini, S. Baroni, V. Blum, D. R. Bowler, A. Bucchini, J. R. Chelikowsky, S. Das, W. Dawson, P. Delugas, M. Dogan, *et al.*, *Modelling and Simulation in Materials Science and Engineering* **31**, 063301 (2023).
 - [9] S. Goedecker, *Reviews of Modern Physics* **71**, 1085 (1999).
 - [10] A. S. Banerjee, L. Lin, W. Hu, C. Yang, and J. E. Pask, *J. Comp. Phys.* **145**, 154101 (2016).
 - [11] A. S. Banerjee, L. Lin, P. Suryanarayana, C. Yang, and J. E. Pask, *Journal of chemical theory and computation* **14**, 2930 (2018).
 - [12] P. Motamarri and V. Gavini, *Physical Review B* **90**, 115127 (2014).
 - [13] L. Lin, A. García, G. Huhs, and C. Yang, *Journal of Physics: Condensed Matter* **26**, 305503 (2014).
 - [14] M. Dogan, K.-H. Liou, and J. R. Chelikowsky, *The Journal of Chemical Physics* **158** (2023).
 - [15] A. S. Banerjee, *Journal of the Mechanics and Physics of Solids* **154**, 104515 (2021).
 - [16] A. S. Banerjee and P. Suryanarayana, *Journal of the Mechanics and Physics of Solids* **96**, 605 (2016).
 - [17] A. M. Lewis, A. Grisafi, M. Ceriotti, and M. Rossi, *Journal of Chemical Theory and Computation* **17**, 7203 (2021).
 - [18] P. B. Jørgensen and A. Bhowmik, *npj Computational Materials* **8**, 183 (2022).
 - [19] L. Zepeda-Núñez, Y. Chen, J. Zhang, W. Jia, L. Zhang, and L. Lin, *Journal of Computational Physics* **443**, 110523 (2021).
 - [20] A. Chandrasekaran, D. Kamal, R. Batra, C. Kim, L. Chen, and R. Ramprasad, *npj Computational Materials* **5**, 22 (2019).
 - [21] L. Fiedler, N. A. Modine, S. Schmerler, D. J. Vogel, G. A. Popoola, A. P. Thompson, S. Rajamanickam, and A. Cangi, *npj Computational Materials* **9**, 115 (2023).
 - [22] F. Brockherde, L. Vogt, L. Li, M. E. Tuckerman, K. Burke, and K.-R. Müller, *Nature communications* **8**, 872 (2017).

- [23] B. G. del Rio, B. Phan, and R. Ramprasad, npj Computational Materials **9**, 158 (2023).
- [24] G. R. Schleder, A. C. Padilha, C. M. Acosta, M. Costa, and A. Fazzio, Journal of Physics: Materials **2**, 032001 (2019).
- [25] H. J. Kulik, T. Hammerschmidt, J. Schmidt, S. Botti, M. A. Marques, M. Boley, M. Scheffler, M. Todorović, P. Rinke, C. Oses, *et al.*, Electronic Structure **4**, 023004 (2022).
- [26] S. Pathrudkar, H. M. Yu, S. Ghosh, and A. S. Banerjee, Physical Review B **105**, 195141 (2022).
- [27] S. Pathrudkar, P. Thiagarajan, S. Agarwal, A. S. Banerjee, and S. Ghosh, npj Computational Materials **10**, 175 (2024).
- [28] S. Pathrudkar, S. Taylor, A. Keripale, A. S. Gangan, P. Thiagarajan, S. Agarwal, J. Marian, S. Ghosh, and A. S. Banerjee, arXiv preprint arXiv:2410.08294 (2024).
- [29] C. Li, O. Sharir, S. Yuan, and G. K. Chan, Nature Communications **16**, 1 (2025).
- [30] Y. S. Teh, S. Ghosh, and K. Bhattacharya, Mechanics of Materials **163**, 104070 (2021).
- [31] R. Ramakrishnan, P. O. Dral, M. Rupp, and O. A. Von Lilienfeld, Scientific data **1**, 1 (2014).
- [32] S. Nandi, T. Vegge, and A. Bhowmik, Scientific data **10**, 783 (2023).
- [33] G. A. Pinheiro, J. Mucelini, M. D. Soares, R. C. Prati, J. L. Da Silva, and M. G. Quiles, The Journal of Physical Chemistry A **124**, 9854 (2020).
- [34] J. Liang, Y. Xu, R. Liu, and X. Zhu, Scientific Data **6**, 213 (2019).
- [35] F. A. Faber, L. Hutchison, B. Huang, J. Gilmer, S. S. Schoenholz, G. E. Dahl, O. Vinyals, S. Kearnes, P. F. Riley, and O. A. Von Lilienfeld, Journal of chemical theory and computation **13**, 5255 (2017).
- [36] J. S. Smith, B. Nebgen, N. Lubbers, O. Isayev, and A. E. Roitberg, The Journal of chemical physics **148** (2018).
- [37] F. Musil, M. J. Willatt, M. A. Langovoy, and M. Ceriotti, Journal of chemical theory and computation **15**, 906 (2019).
- [38] A. Jain, S. P. Ong, G. Hautier, W. Chen, W. D. Richards, S. Dacek, S. Cholia, D. Gunter, D. Skinner, G. Ceder, *et al.*, APL materials **1** (2013).
- [39] J. E. Saal, S. Kirklin, M. Aykol, B. Meredig, and C. Wolverton, Jom **65**, 1501 (2013).
- [40] A. Jain, J. Montoya, S. Dwaraknath, N. E. Zimmermann, J. Dagdelen, M. Horton, P. Huck, D. Winston, S. Cholia, S. P. Ong, *et al.*, Handbook of Materials Modeling: Methods: Theory and Modeling, 1751 (2020).
- [41] K. Li, D. Persaud, K. Choudhary, B. DeCost, M. Greenwood, and J. Hattrick-Simpers, Nature Communications **14**, 7283 (2023).
- [42] Q. Li, N. Fu, S. S. Omeel, and J. Hu, npj Computational Materials **10**, 245 (2024).
- [43] D. Chen, Z. Li, Y. Ni, G. Zhang, D. Wang, Q. Liu, S. Wu, J. Yu, and L. Wang, Advances in Neural Information Processing Systems **37**, 18036 (2024).
- [44] T. Blesgen, V. Gavini, and V. Khoromskaia, Journal of computational physics **231**, 2551 (2012).
- [45] P. Motamarri, V. Gavini, and T. Blesgen, Physical Review B **93**, 125104 (2016).
- [46] C. Feng, Y. Zhang, and B. Jiang, Journal of Chemical Theory and Computation (2025).
- [47] B. Focassio, M. Domina, U. Patil, A. Fazzio, and S. Sanvito, npj Computational Materials **9**, 87 (2023).
- [48] E. Prodan and W. Kohn, Proceedings of the National Academy of Sciences **102**, 11635 (2005).
- [49] W. Kohn, Physical Review Letters **76**, 3168 (1996).
- [50] M. Benzi, N. Razouk, *et al.*, Electron. Trans. Numer. Anal **28**, 08 (2007).
- [51] M. Benzi, P. Boito, and N. Razouk, SIAM review **55**, 3 (2013).
- [52] R. Baer and M. Head-Gordon, Physical review letters **79**, 3962 (1997).
- [53] P. Suryanarayana, Chemical Physics Letters **679**, 146 (2017).
- [54] S. Mohr, L. E. Ratcliff, L. Genovese, D. Caliste, P. Boulanger, S. Goedecker, and T. Deutsch, Physical Chemistry Chemical Physics **17**, 31360 (2015).
- [55] F. Shimojo, R. K. Kalia, A. Nakano, and P. Vashishta, Computer Physics Communications **140**, 303 (2001).
- [56] P. Suryanarayana, P. P. Pratapa, A. Sharma, and J. E. Pask, Computer Physics Communications **224**, 288 (2018).
- [57] A. Nakata, J. S. Baker, S. Y. Mujahed, J. T. Poulton, S. Arapan, J. Lin, Z. Raza, S. Yadav, L. Truflandier, T. Miyazaki, *et al.*, The Journal of chemical physics **152** (2020).
- [58] C. García-Cervera, J. Lu, Y. Xuan, and W. E, Physical Review B—Condensed Matter and Materials Physics **79**, 115110 (2009).
- [59] C.-K. Skylaris, P. D. Haynes, A. A. Mostofi, and M. C. Payne, The Journal of chemical physics **122** (2005).
- [60] J. Kaplan, S. McCandlish, T. Henighan, T. B. Brown, B. Chess, R. Child, S. Gray, A. Radford, J. Wu, and D. Amodei, arXiv preprint arXiv:2001.08361 (2020).
- [61] J. Hestness, S. Narang, N. Ardalani, G. Diamos, H. Jun, H. Kianinejad, M. M. A. Patwary, Y. Yang, and Y. Zhou, arXiv preprint arXiv:1712.00409 (2017).
- [62] B. Sorscher, R. Geirhos, S. Shekhar, S. Ganguli, and A. Morcos, Advances in Neural Information Processing Systems **35**, 19523 (2022).
- [63] X. Zhai, A. Kolesnikov, N. Houlsby, and L. Beyer, in *Proceedings of the IEEE/CVF conference on computer vision and pattern recognition* (2022) pp. 12104–12113.
- [64] H. Tan, S. Wu, F. Du, Y. Chen, Z. Wang, F. Wang, and X. Qi, Advances in Neural Information Processing Systems **36** (2024).
- [65] M. Paul, S. Ganguli, and G. K. Dziugaite, Advances in neural information processing systems **34**, 20596 (2021).
- [66] M. Toneva, A. Sordoni, R. T. d. Combes, A. Trischler, Y. Bengio, and G. J. Gordon, arXiv preprint arXiv:1812.05159 (2018).
- [67] M. He, S. Yang, T. Huang, and B. Zhao, in *Proceedings of the IEEE/CVF Conference on Computer Vision and Pattern Recognition* (2024) pp. 7713–7722.
- [68] H. Zheng, R. Liu, F. Lai, and A. Prakash, Coverage-centric coreset selection for high pruning rates (2023), arXiv:2210.15809 [cs.LG].
- [69] O. Sener and S. Savarese, Active learning for convolutional neural networks: A core-set approach (2018), arXiv:1708.00489 [stat.ML].
- [70] X. Xia, J. Liu, J. Yu, X. Shen, B. Han, and T. Liu, in *The Eleventh International Conference on Learning Representations* (2022).
- [71] S. Yang, Z. Xie, H. Peng, M. Xu, M. Sun, and P. Li, arXiv preprint arXiv:2205.09329 (2022).
- [72] B. Mirzasoleiman, J. Bilmes, and J. Leskovec, in *International Conference on Machine Learning* (PMLR, 2020)

- pp. 6950–6960.
- [73] K. Killamsetty, G. Ramakrishnan, A. De, and R. Iyer, in *International Conference on Machine Learning* (PMLR, 2021) pp. 5464–5474.
 - [74] K. Killamsetty, D. Sivasubramanian, G. Ramakrishnan, and R. Iyer, in *Proceedings of the AAAI Conference on Artificial Intelligence*, Vol. 35 (2021) pp. 8110–8118.
 - [75] K. Killamsetty, X. Zhao, F. Chen, and R. Iyer, *Advances in neural information processing systems* **34**, 14488 (2021).
 - [76] S. Yang, Z. Cao, S. Guo, R. Zhang, P. Luo, S. Zhang, and L. Nie, in *Forty-first International Conference on Machine Learning* (2024).
 - [77] C. Guo, B. Zhao, and Y. Bai, in *International Conference on Database and Expert Systems Applications* (Springer, 2022) pp. 181–195.
 - [78] R. M. Martin, *Electronic Structure: Basic Theory and Practical Methods*, 1st ed. (Cambridge University Press, 2004).
 - [79] Q. Xu, A. Sharma, B. Comer, H. Huang, E. Chow, A. J. Medford, J. E. Pask, and P. Suryanarayana, *SoftwareX* **15**, 100709 (2021).
 - [80] Q. Xu, A. Sharma, and P. Suryanarayana, *SoftwareX* **11**, 100423 (2020).
 - [81] S. Ghosh and P. Suryanarayana, *Computer Physics Communications* **212**, 189 (2017).
 - [82] D. Hamann, *Physical Review B* **88**, 085117 (2013).
 - [83] M. Schlipf and F. Gygi, *Computer Physics Communications* **196**, 36 (2015).
 - [84] M. J. Van Setten, M. Giantomassi, E. Bousquet, M. J. Verstraete, D. R. Hamann, X. Gonze, and G.-M. Rignanese, *Computer Physics Communications* **226**, 39 (2018).
 - [85] J. P. Perdew, K. Burke, and M. Ernzerhof, *Physical review letters* **77**, 3865 (1996).
 - [86] A. S. Banerjee, P. Suryanarayana, and J. E. Pask, *Chemical Physics Letters* **647**, 31 (2016).
 - [87] D. J. Evans and B. L. Holian, *The Journal of chemical physics* **83**, 4069 (1985).
 - [88] C. Chen, Y. Zuo, W. Ye, X. Li, and S. P. Ong, *Nature Computational Science* **1**, 46 (2021).
 - [89] C. Chen and S. P. Ong, *Nature Computational Science* **2**, 718 (2022).
 - [90] A. Grisafi, A. Fabrizio, B. Meyer, D. M. Wilkins, C. Corminboeuf, and M. Ceriotti, *ACS central science* **5**, 57 (2018).
 - [91] A. Fabrizio, A. Grisafi, B. Meyer, M. Ceriotti, and C. Corminboeuf, *Chemical science* **10**, 9424 (2019).
 - [92] D. Hendrycks and K. Gimpel, *arXiv preprint arXiv:1606.08415* (2016).
 - [93] D. P. Kingma and J. Ba, *arXiv preprint arXiv:1412.6980* (2014).
 - [94] I. Loshchilov and F. Hutter, *arXiv preprint arXiv:1711.05101* (2017).
 - [95] K. R. Briling, A. Fabrizio, and C. Corminboeuf, *The Journal of Chemical Physics* **155** (2021).
 - [96] J. M. Alred, K. V. Bets, Y. Xie, and B. I. Yakobson, *Composites Science and Technology* **166**, 3 (2018).
 - [97] J. Harris, *Physical Review B* **31**, 1770 (1985).
 - [98] W. M. C. Foulkes and R. Haydock, *Physical review B* **39**, 12520 (1989).

V. SUPPLEMENTAL MATERIALS

A. Error Metrics

The normalized root mean square error (NRMSE) of the ML predicted electron density is defined as

$$NRMSE = \frac{\sqrt{\frac{1}{N} \sum_{i=1}^N (\rho_{DFT}^i - \rho_{ML}^i)^2}}{\rho_{DFT}^{max} - \rho_{DFT}^{min}} \quad (3)$$

where N is the number of grid-points for each snapshot. At i -th grid point, ρ_{DFT}^i represents the electron density calculated using KS-DFT while ρ_{ML}^i represents the electron density predicted by the ML models. ρ_{DFT}^{max} and ρ_{DFT}^{min} are the maximum and minimum values of electron density across all grid-points of that snapshot.

Let u is the error field of the ML-predicted electron density, given by $u(x) = \rho_{DFT}(x) - \rho_{ML}(x)$, with $x \in \Omega$. The H^1 seminorm of the scalar error field $u(x)$ over a domain Ω is defined as $|u|_{H^1(\Omega)} = (\int_{\Omega} |\nabla u(x)|^2 dx)^{1/2}$. The H^1 norm is defined as $\|u\|_{H^1(\Omega)} = \left(\|u\|_{L^2(\Omega)}^2 + |u|_{H^1(\Omega)}^2 \right)^{1/2}$. These quantities are well defined whenever, u lies in the Sobolev space $H^1(\Omega)$.

In the paper, the energy prediction errors are defined as the absolute differences (in Hartree per atom) between KS-DFT energies and the energies obtained by postprocessing the ML-predicted electron density.

B. Experimental Details

Dataset details: We use sufficiently large datasets to achieve high accuracy in ML for all three material systems. The KS-DFT dataset for the aluminum system consists of 200 training snapshots (216,000 grid points each), totaling 43.2×10^6 grid points, obtained from a 32-atom simulation cell; the test set includes 60 snapshots from six temperatures. The dataset for CrFeCoNi system, taken from 69 compositions, consists of 140 training snapshots (totaling 40.9×10^6 grid points) and test set includes 207 test snapshots from four different temperatures and 69 compositions, also from a 32-atom simulation cell. The dataset for water includes 112 training snapshots (456,533 grid points each, totaling 51.1×10^6 grid points), and 193 test snapshots from four temperatures, obtained from a 32-atom simulation cell.

Neural Network: We employ a deep neural network with 12 hidden layers, each containing 900 nodes, using GELU activation [92] in the hidden layers and a ReLU activation in the output layer. A learning rate of 0.001 is used across all cases, with the AdamW optimizer [93, 94].

GraNd score computation: The epoch 10, 10 and 30 are chosen for GraNd score computation for Aluminum,

CrFeCoNi and water respectively. Figure 13 shows the errors on the test dataset for Aluminum, CrFeCoNi and water for pruned subsets, for scores computed at different times in training. The Figure 13 shows that the computing scores early in training is sufficient to identify important examples, aligning with the findings of [65].

Hyper-parameters for CCS: There are two hyper-parameters for the CCS method. a) the hard cut-off rate (β) and b) the number of strata (k). The optimal β increases with the pruning rate. The performance of various CCS-based coresets constructed from varying β is shown in Figure 12. The error in charge density prediction for various number of strata, k is shown in Figure 11. The error is not very sensitive to the that the number of strata(k), which is consistent with the findings of Zheng et al. [68] for image classification datasets. Hence, in this work, the number of strata(k) being used is 100 all three material systems for all pruning factors.

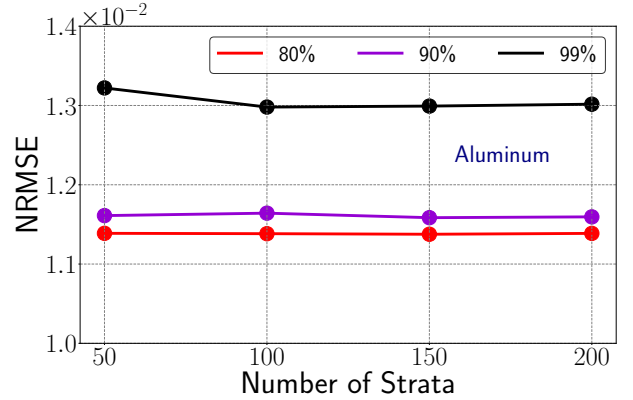


FIG. 11: Plots showing the error in electron density prediction with various numbers of strata for Aluminum system for various pruning factors for CCS method.

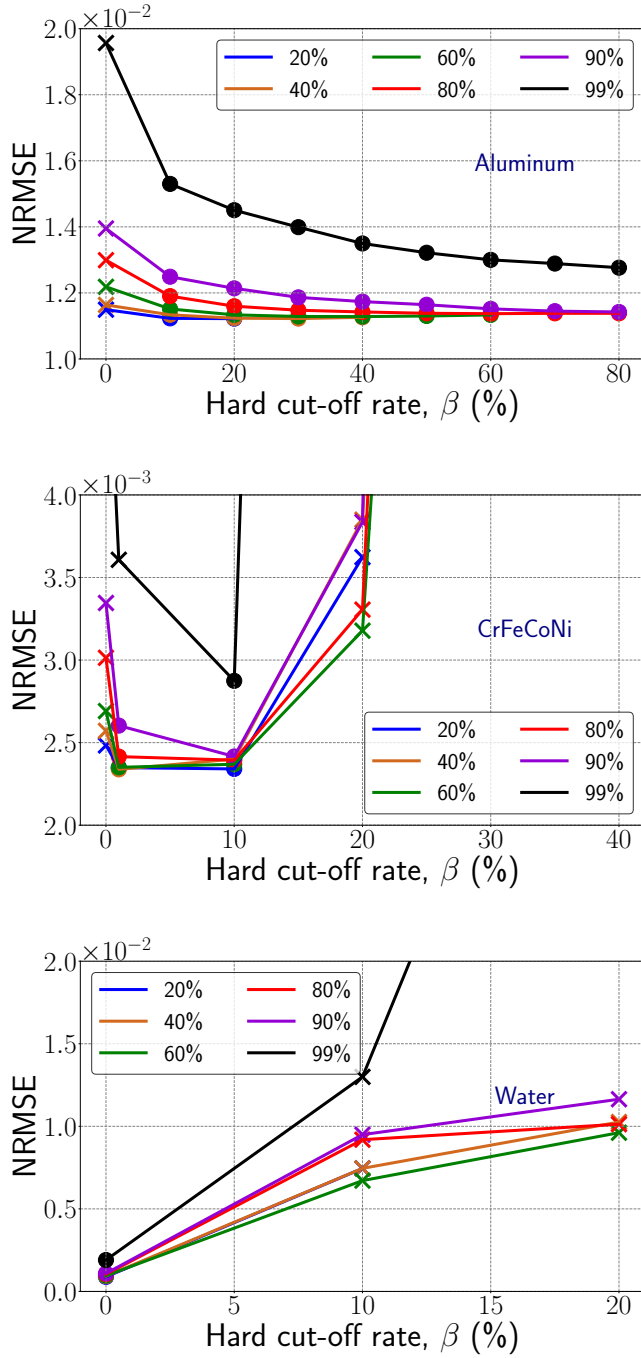


FIG. 12: Plots showing the error in electron density prediction with varying β for (Top) Aluminum, (Middle) CrFeCoNi and (Bottom) water system for the CCS based pruning. It is observed that the obtained NRMSE with pruned dataset vary with the choice of β . For higher pruning rate, a higher β may be optimal. The points with \times markers failed to beat random pruning.

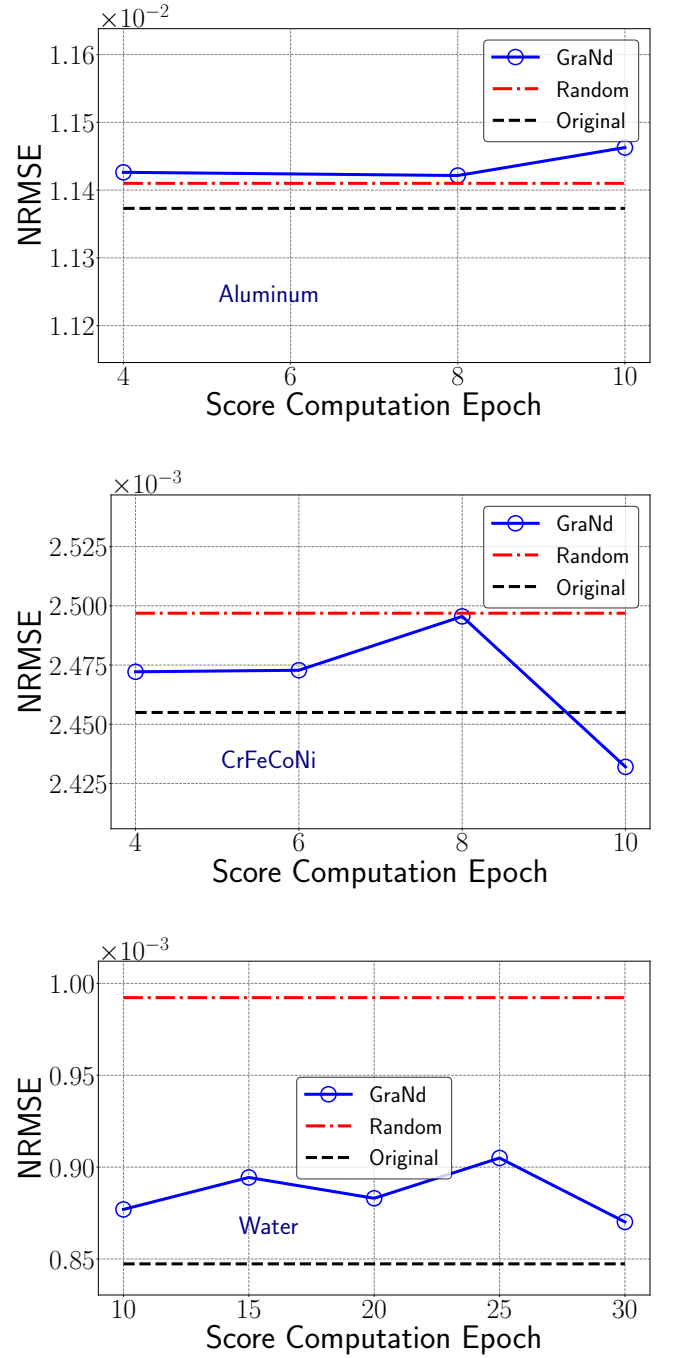


FIG. 13: Plots showing the error in electron density prediction for (Top) Aluminum(20% pruning), (Middle) CrFeCoNi(40% pruning) and (Bottom) Water(40% pruning) after computing the GraNd score at different times in training.

C. Additional Results

A complete and unscaled view of the error versus pruning factor for CrFeCoNi and water, corresponding to Fig-

ure 6 and Figure 8, is provided in Figure 14 and Figure 15 for completeness. It shows that the GraNd method becomes too erroneous beyond 60% pruning for both CrFeCoNi and water. However, the random pruning provides high accuracy up to 90%.

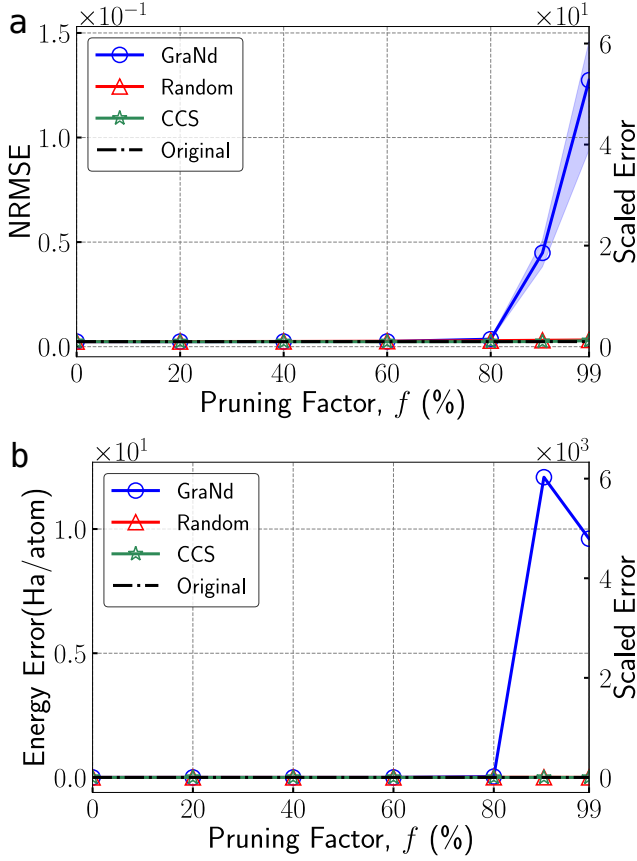


FIG. 14: **CrFeCoNi system:** (a) Error in the predicted electron density for various pruning factors. (b) Error in energy obtained from the predicted electron density for various pruning factors.

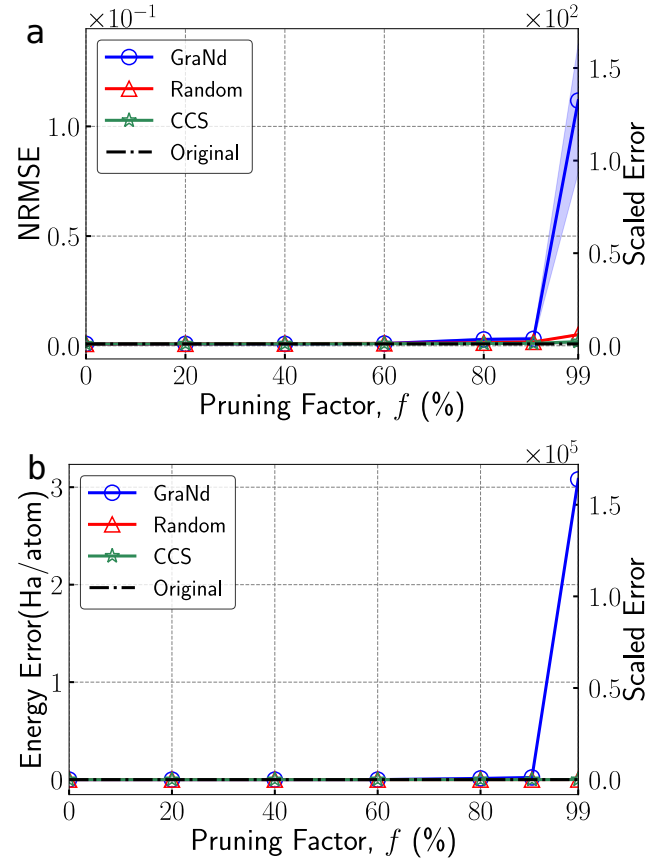


FIG. 15: **Water system:** (a) Error in the predicted electron density for various pruning factors. (b) Error in energy obtained from the predicted electron density for various pruning factors.

D. Quantifying the coverage of a specific distribution by a subset

The GraNd score and other state-of-the-art importance-based pruning methods often perform poorly at higher pruning rates because of poor data coverage.

We have evaluated the AUC_{pr} by computing the expected minimum distance from the data in the validation dataset to the data in coreset.

Aluminum				
Pruning Rate	AUC_{pr}		NRMSE	
	GraNd	CCS	GraNd	CCS
90%	8.396	8.30	1.58×10^{-2}	1.15×10^{-2}
99%	8.727	8.584	2.55×10^{-2}	1.3×10^{-2}
CrFeCoNi				
Pruning Rate	AUC_{pr}		NRMSE	
	GraNd	CCS	GraNd	CCS
90%	13.074	13.039	4.4×10^{-2}	2.4×10^{-3}
99%	13.416	13.335	1.27×10^{-1}	2.88×10^{-3}
Water				
Pruning Rate	AUC_{pr}		NRMSE	
	GraNd	CCS	GraNd	CCS
90%	23.18	22.93	3.1×10^{-2}	1.09×10^{-3}
99%	25.29	24.89	1.11×10^{-1}	1.9×10^{-3}

TABLE I: Comparison of AUC_{pr} and NRMSE between GraNd and CCS method for different pruning percentages

From the Table I, we can see that, for 90% and 99% pruning percentage, the CCS has lower AUC_{pr} than the GraNd method. It confirms that the CCS method based coreset indeed selects a subset that ensures a better data coverage, as evidenced by its lower errors (NRMSE).

E. Generalizability

In this section, we provide additional results that demonstrate the generalizability of ML models trained on pruned datasets. The error in electron density prediction for defects in the Aluminum-108 system is shown in Figure 16. The generalization error of the GraNd method increases rapidly beyond 60% pruning, whereas random pruning maintains high accuracy up to 90% pruning. The CCS method supports a remarkably high pruning factor (99%) without any significant loss in generalization performance. For CrFeCoNi system with defects, the errors in electron density prediction for defects is shown in Figure 17. The generalization performance for GraNd worsen rapidly beyond 40%, whereas random pruning maintains high accuracy up to 80% pruning factors. However, CCS maintains near-original performance until 99% pruning. We plot the ML-predicted electron density fields obtained from the original dataset, 90% CCS dataset and 99% CCS dataset in Figure 18 and com-

pare against KS-DFT calculations. It demonstrates that the CCS-based pruning, even at two orders of magnitude reduction, retains a remarkably high level of the original model’s generalization capability.

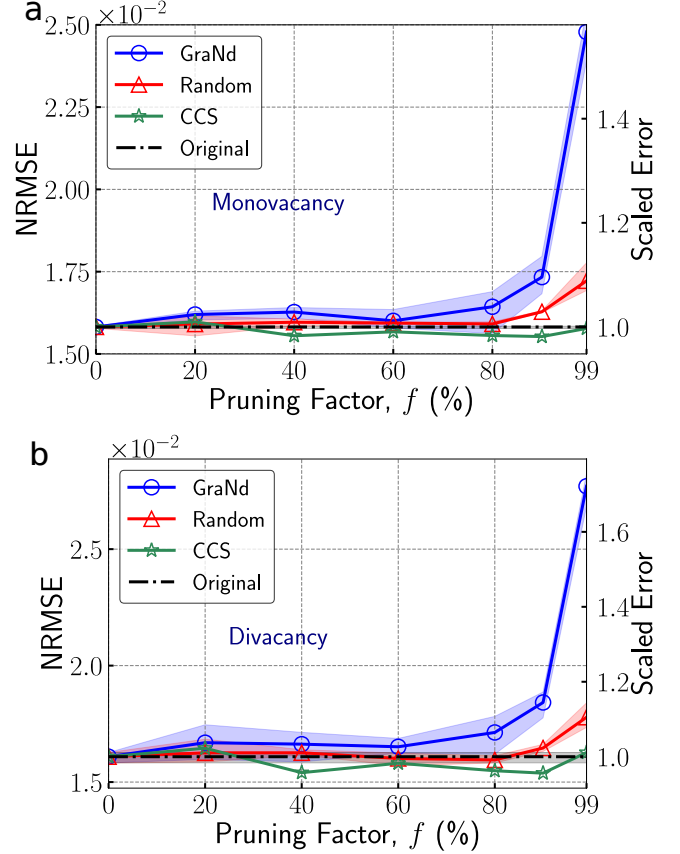


FIG. 16: **Generalizability tests for Aluminum system:** The error in the electron density prediction for various pruning factors for (a) monovacancies (b) divacancies for Aluminum 108 atoms system. The shaded region represents the range (maximum to minimum) of three ML models around the mean, shown by a solid line.

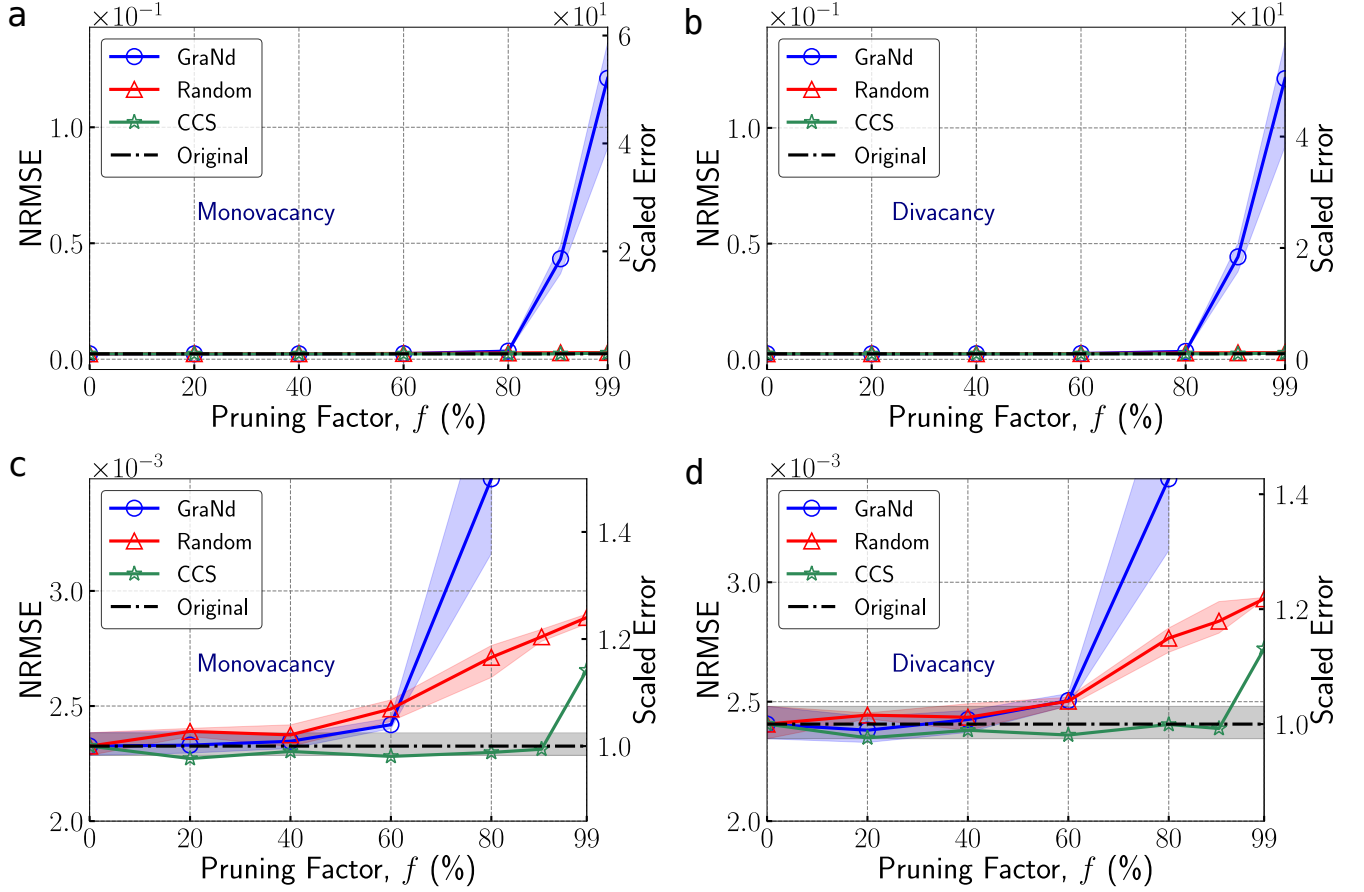


FIG. 17: **Generalizability tests for CrFeCoNi system:** The error in the electron density prediction for various pruning factors for (a) monovacancy defects. (b) divacancy defects for CrFeConi 32 atoms system. The shaded region represents the range (maximum to minimum) of three ML models around the mean, shown by a solid line. Figures(c-d) shows the magnified view of the Figures(a-b)

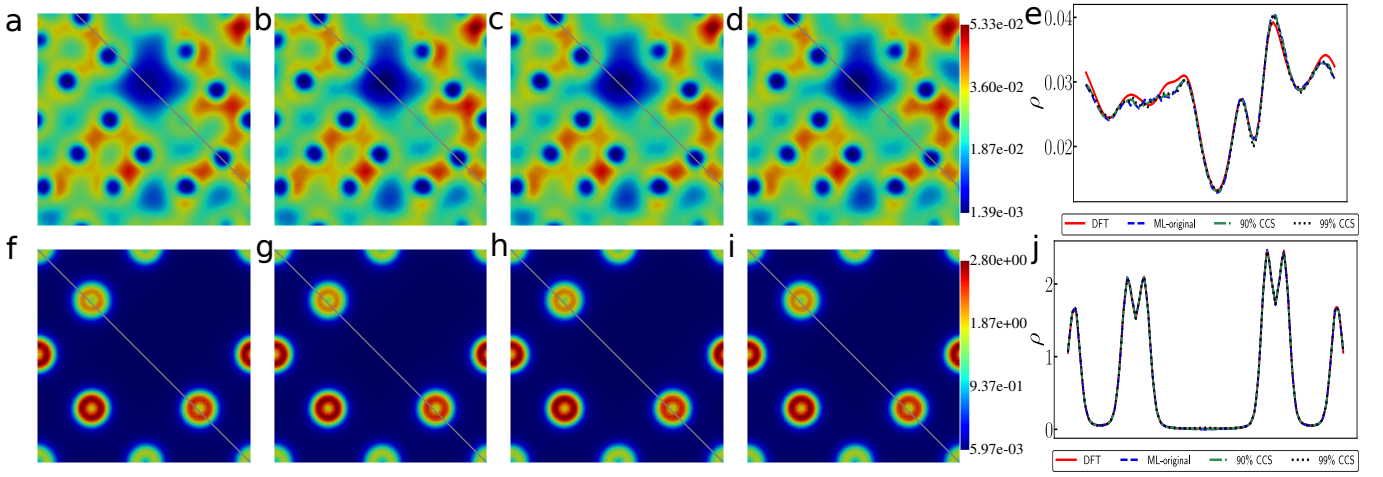


FIG. 18: **Model generalizability to unseen defect configurations:** (*Top*) Di-vacancy defect for Aluminum 108 atoms systems. Two-dimensional(2D) slices of electron density obtained by: (a) DFT and (b-d) ML model trained on the original dataset, 90% CCS and 99% CCS based pruned dataset. (e) Electron density along the solid line, shown in Figures (a-d). (*Bottom*) Di-vacancy defect for CrFeCoNi 32 atoms systems. 2D slices of electron density obtained by: (f) DFT and (g-i) ML model trained on the original dataset, 90% CCS and 99% CCS based pruned dataset. (j) Electron density along the solid line, shown in Figures (f-i). The unit of electron density is $e \cdot \text{Bohr}^{-3}$, where e denotes the electronic charge.

F. Postprocessing of ML predicted electron density

For application purposes, it is of interest to compute downstream properties from the ML-predicted electron density. Since the Kohn-Sham total ground-state energy is a key property that can be computed from the electron density, it can serve as a useful test for the downstream accuracy of the ML model. We postprocess the density predictions to obtain the corresponding total ground-state energies as follows. The predicted electron density is first rescaled by the total number of electrons; this serves to ensure that the total electronic charge is consistent [26, 27, 95, 96]. The scaled electron density ρ^{scaled} at grid point \mathbf{r} is obtained from the predicted electron density ρ^{ML} via:

$$\rho^{\text{scaled}}(\mathbf{r}) = \rho^{\text{ML}}(\mathbf{r}) \frac{N_e}{\int_{\Omega} \rho^{\text{ML}}(\mathbf{r}) d\mathbf{r}}. \quad (4)$$

Here Ω is the periodic supercell used in the calculations, and N_e is the number of electrons in the system. The rescaled electron density ρ^{scaled} is then used to set up the Kohn-Sham Hamiltonian and a single diagonalization step is performed by using the same electronic structure calculation framework, as was used in the data generation process [79–81]. Thereafter, the energy of the system is computed using the Harris-Foulkes formula [97, 98]. The difference between the energy obtained from the ML-predicted electron density and that obtained from the original DFT density serve as the energy error reported in this work.

G. Timing Comparison

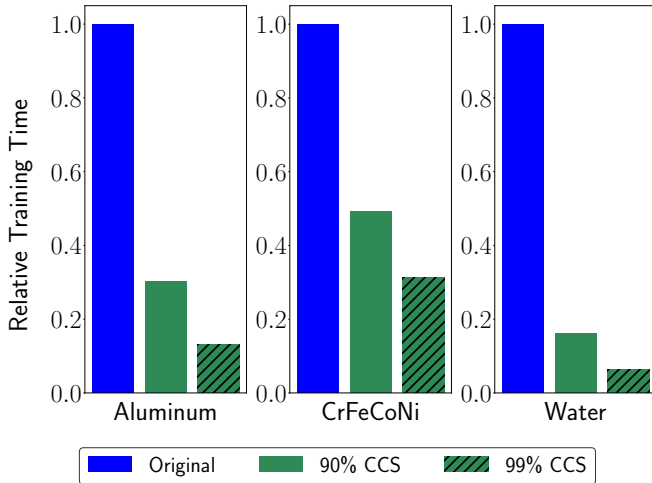


FIG. 19: Training Time comparison between the Original ML model, 90% CCS and 99% CCS based pruned dataset

Pruned subsets speed up the training process significantly, as shown in Figure 19. Training with 90% CCS-pruned subsets reduces training time by 70%, 50% and 84% for Aluminum, CrFeCoNi and Water respectively, while matching the original models’ predictive performance. 99% CCS-based pruned subsets reduces the training time further, while also suffering nominal increase in NRMSE.

H. Isosurface Plots

The 3D electron density fields are shown as iso-surface plots for the three materials in Figures 20, 22, and 24. The overall pattern of electron density iso-surfaces is well captured by the original, 90%, and 99% pruned datasets. The corresponding 3D error fields are shown in Figures 21, 23, and 25. Although the error iso-surfaces closely resemble those of the original data even after 90% and 99% pruning, a slight yet progressive increase in error is observed as pruning levels increase.

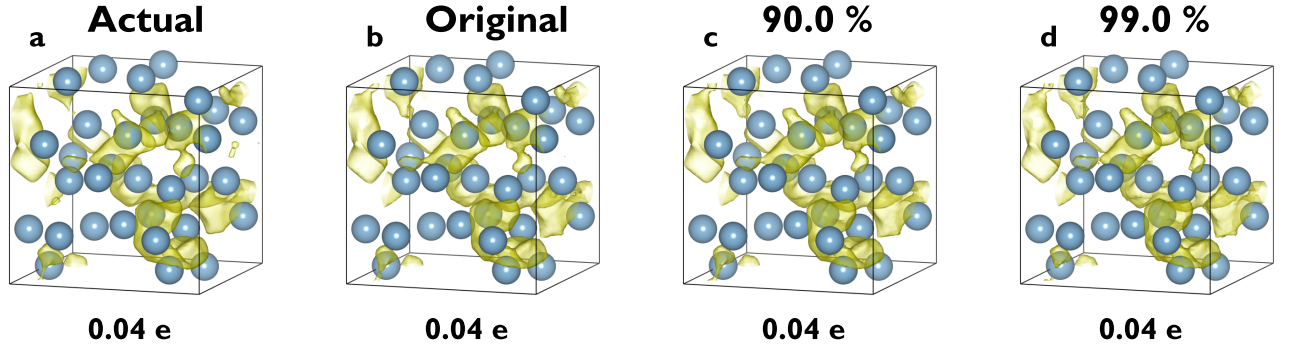


FIG. 20: Aluminum system at 1500 K. Iso-surfaces of electron density obtained by KS-DFT (a) and ML model for original (unpruned) (b), 90% CCS (c), and 99% CCS (d).

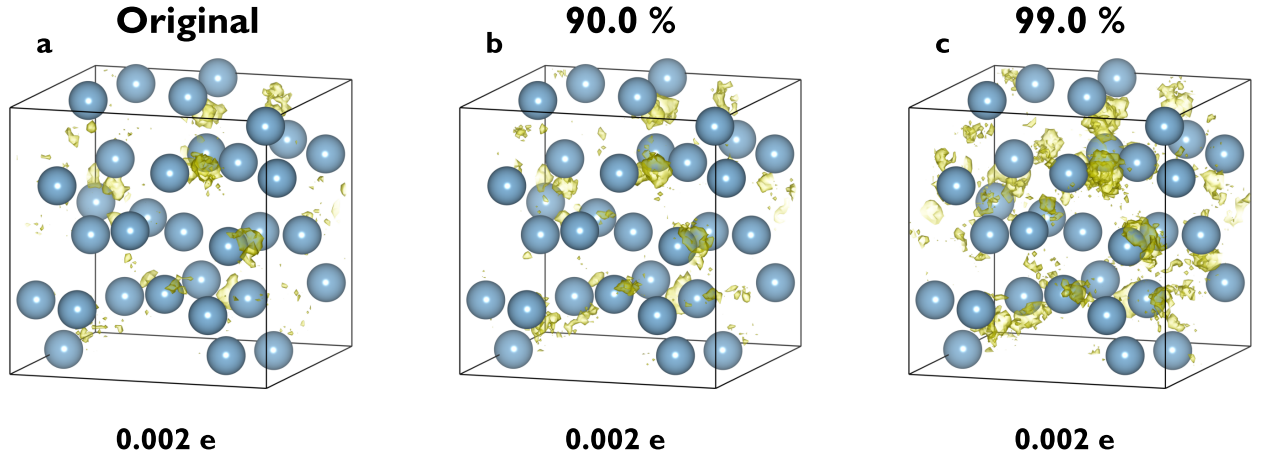


FIG. 21: Aluminum system at 1500 K. Iso-surfaces of errors in electron density obtained by ML model for original (a), 90% CCS (b), and 99% CCS(c) respectively.

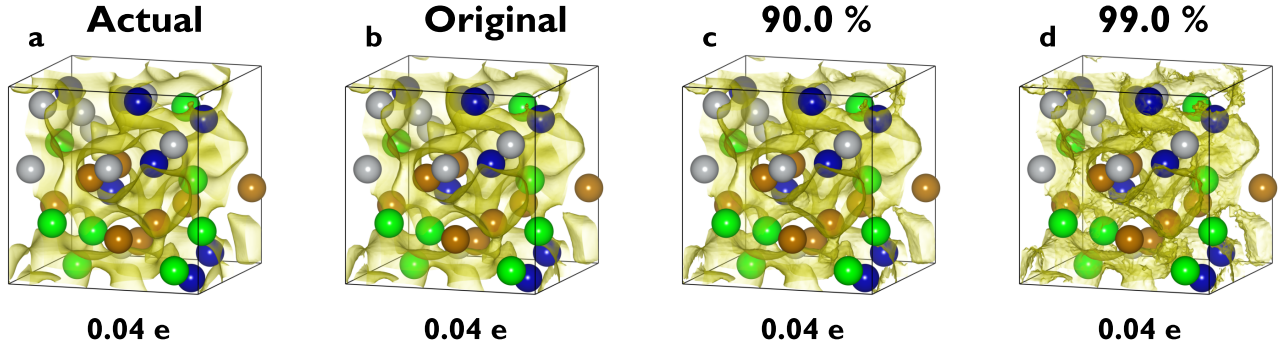


FIG. 22: $\text{Cr}_{25}\text{Fe}_{25}\text{Co}_{25}\text{Ni}_{25}$ system at 5000K: Iso-surfaces of electron density obtained by DFT (a) and ML model for original (unpruned) (b), 90% CCS (c), and 99.5% CCS (d). The green, orange, blue, and gray spheres represent the Cr, Fe, Co, and Ni atoms.

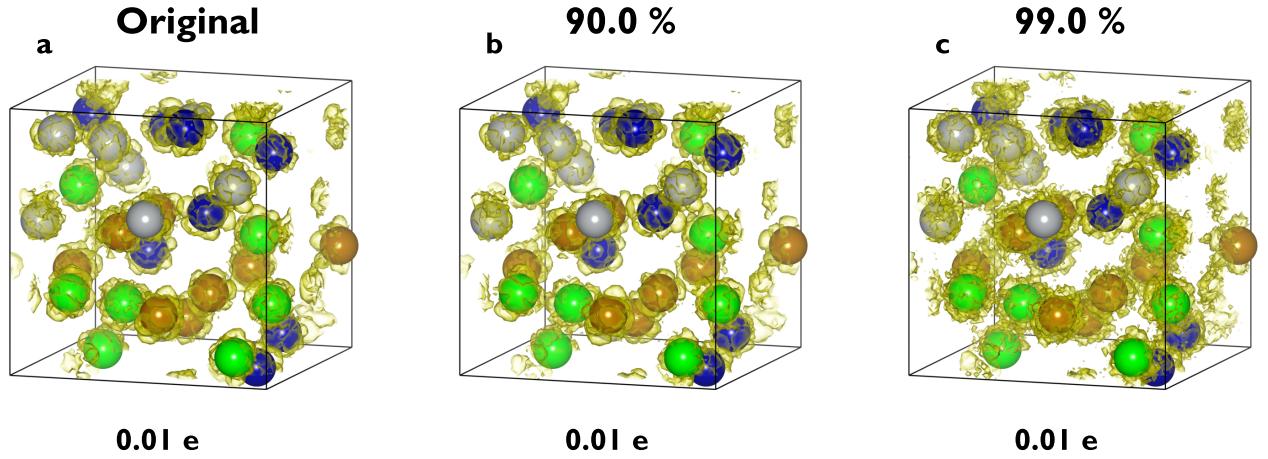


FIG. 23: $\text{Cr}_{25}\text{Fe}_{25}\text{Co}_{25}\text{Ni}_{25}$ system at 5000K: Iso-surfaces of errors in electron density obtained by ML model for original (a), 90% CCS (b), and 99.5% CCS (c) respectively.

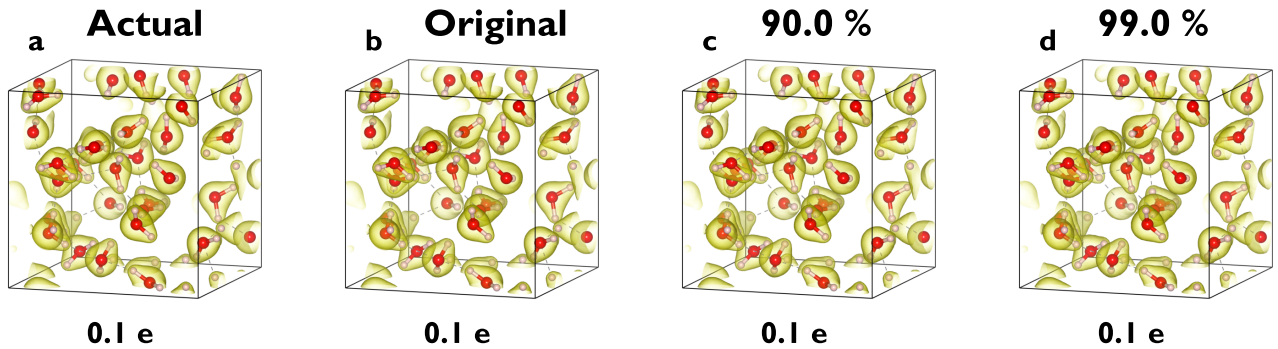


FIG. 24: **Water system at 600K**: Iso-surfaces of electron density (at 0.1 e) obtained by DFT (a) and ML model for original (b), 90% CCS (c), and 99.5% CCS (d). The red and pink spheres represent the Oxygen and Hydrogen atoms.

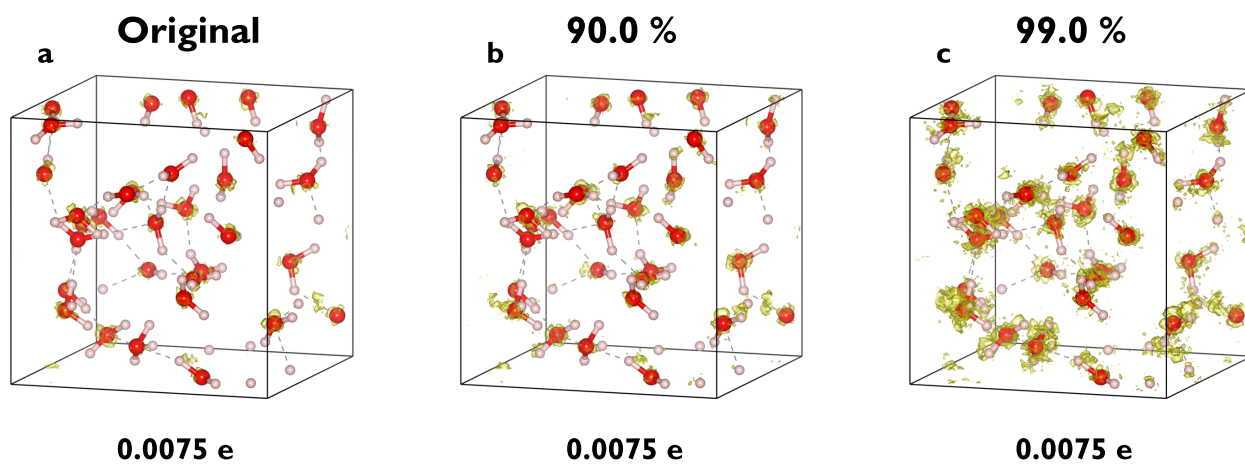


FIG. 25: **Water system at 600K**: Iso-surfaces of errors in electron density (at 0.0075 e) obtained by ML model for original (unpruned) (a), 90% CCS (b), and 99.5% CCS (c) respectively.